University of Alberta

Exclusive Interactions in $p\bar{p}$ Collisions at $\sqrt{s} = 1.96$ TeV

by

Andrew Hamilton

A thesis submitted to the Faculty of Graduate Studies and Research in partial fulfillment of the requirements for the degree of **Doctor of Philosophy**.

Department of Physics

Edmonton, Alberta
Fall 2006

Your file Votre référence
ISBN: 978-0-494-23039-8
Our file Notre référence
ISBN: 978-0-494-23039-8

Abstract

This thesis presents two exclusive production processes in $p\bar{p}$ collisions at $\sqrt{s} = 1.96$ TeV, using the Collider Detector Facility at Fermi National Accelerator Laboratory. An observation of exclusive e^+e^- production through $\gamma\gamma \rightarrow e^+e^-$ is presented, as well as evidence for exclusive production of $\gamma\gamma$ through $gg \rightarrow \gamma\gamma$ (via a quark loop). The exclusive e^+e^- production observation is based on 16 candidate events, with a background estimate of $2.1^{+0.7}_{-0.3}$. Each event has an e^+e^- pair ($E_T(e) > 5$ GeV, $|\eta(e)| < 2$) and nothing else observable in the CDF detector. The measured cross section is $1.6\ ^{+0.5}_{-0.3}$(stat) ± 0.3(sys) pb, while the predicted cross section is 1.711 ± 0.008 pb. The kinematic properties of the events are consistent with the predictions of the LPAIR Monte Carlo. The evidence for exclusive $\gamma\gamma$ production consists of 3 candidate events, with a background estimate of $0.0^{+0.2}_{-0.0}$ events. Each event has two photons ($E_T(\gamma) > 5$ GeV, $|\eta(\gamma)| < 1$) and nothing else observable in the CDF detector. The measured cross section for these events is $0.14\ ^{+0.14}_{-0.04}$ (stat) $\pm\ 0.03$ (sys) pb. It agrees with the theoretical prediction of 0.04 pb with a factor 3 to 5 theoretical uncertainty.

Acknowledgements

In my 22 years of schooling, some teachers taught me what I really need to know. Dr. Roman Koniuk, without your passion for the fundamental understanding of nature, I might not be in physics at all. Dr. Sampa Bhadra, your endless energy and commitment to you students gave me the confidence and opportunity to persue graduate studies. Dr. W. John McDonald, your commitment to the pure analytical nature of science is truly unique, I hope to someday to be half the scientist you are. Dr. James Pinfold, thank-you for teaching me that research is a delicate balance between knowledge, inspiration, politics, and confidence in your own ideas. Dr. Michael Albrow, in 30 years, if I am as excited about particle physics as you have taught me to be, I will have had a fulfilling career.

Of course, my family has done their fair share of teaching as well. Mom, John, and Don, I would not be the person I am without you as my parents. Thank-you for the upbringing you gave me and the support you continue to give me. Jessie and Wally, thank-you for all your support throughout my graduate studies. Your kindness has far exceeded any expectations. Kelleigh, thank-you for your commitment to me and my career, this degree is as much yours as it is mine. You have taught me more in our seven years together than all my 22 years of schooling combined.

Thank-you to everyone at CDF, this work would not have been possible without the dedication of all my collaborators. To those I worked with; Mary Convery, Ray Culbertson, Dino Goulianos, Beate Heinemann, Regis Lefevre, Koji Terashi, and Angela Wyatt, your help was invaluable to me.

I also thank the Fermilab staff and the technical staffs of the participating institutions for their vital contributions. This work was supported by the U.S. Department of Energy and National Science Foundation; the Italian Istituto Nazionale di Fisica Nucleare; the Ministry of Education, Culture, Sports, Science and Technology of Japan; the Natural Sciences and Engineering Research Council of Canada; the Swiss National Science Foundation; the A.P. Sloan Foundation; the Bundesministerium fuer Bildung und Forschung, Germany; the Particle Physics and Astronomy Research Council and the Royal Society, UK; the Russian Foundation for Basic Research; the Comision Interministerial de Ciencia y Tecnologia, Spain; in part by the European Community's Human Potential Programme under contract HPRN-CT-2002-00292; and the Academy of Finland.

To Kelleigh.
What you have taught me is more valuable than any degree. I love you.

Contents

1 Theory and Motivation 1
- 1.1 The Standard Model . . . 1
  - 1.1.1 Quantum Electrodynamics . . . 2
  - 1.1.2 Electroweak Theory . . . 3
  - 1.1.3 Quantum Chromodynamics . . . 4
  - 1.1.4 The Higgs Boson . . . 5
  - 1.1.5 Beyond the Standard Model . . . 6
- 1.2 Exclusive Interactions . . . 7
  - 1.2.1 QED Mediated Exclusive Interactions . . . 8
  - 1.2.2 QCD Mediated Exclusive Interactions . . . 9
- 1.3 Why are Exclusive Interactions Interesting? . . . 11
- 1.4 Other Related Work at CDF . . . 14
- 1.5 Outline of Analysis Procedure . . . 15

2 Accelerator and Detector 16
- 2.1 Accelerator Complex . . . 16
- 2.2 CDF Detector . . . 18
  - 2.2.1 Tracking Detectors . . . 19
  - 2.2.2 Calorimeters . . . 21
  - 2.2.3 Cherenkov Luminosity Counter . . . 27
  - 2.2.4 Beam Shower Counters . . . 27
  - 2.2.5 Muon Chambers . . . 28
  - 2.2.6 Trigger . . . 29

3 Observation of Exclusive e^+e^- Production 31
- 3.1 Event Selection . . . 31
  - 3.1.1 Trigger and Good Run List . . . 31
  - 3.1.2 Electron ID Cuts . . . 32
  - 3.1.3 Cosmic Cut . . . 34
  - 3.1.4 Exclusivity Cuts . . . 34
  - 3.1.5 Track Cut . . . 39
  - 3.1.6 Signal Sample . . . 39
- 3.2 Efficiencies . . . 43
  - 3.2.1 Electron Efficiency . . . 43
  - 3.2.2 Final State Radiation Efficiency, ε_{fsr} . . . 51

3.2.3 Cosmic Efficiency, ε_{cos} 52
3.2.4 Exclusive Efficiency 54
3.3 Backgrounds 58
3.3.1 'Jet' Fake Background 59
3.3.2 Cosmic Background 60
3.3.3 Exclusivity Background 60
3.3.4 Dissociation Background 62
3.3.5 Background Summary 65
3.4 Cross Section 66

4 Evidence of Exclusive $\gamma\gamma$ Production **67**
4.1 Event Selection 67
4.1.1 Trigger and Good Run Lists 67
4.1.2 Photon ID Cuts 67
4.1.3 Cosmic Ray Cut 68
4.1.4 Exclusivity Cuts 68
4.1.5 Track Cut 68
4.1.6 Signal Sample 68
4.1.7 Signal Sample Discussion 72
4.2 Efficiencies 72
4.2.1 Conversion Efficiency 73
4.3 Backgrounds 73
4.3.1 Jet Fake Background 74
4.3.2 Exclusivity Background 75
4.3.3 Dissociation Background 76
4.3.4 Indistinquishable Physics Processes 77
4.3.5 Background Summary 77
4.4 Cross Section 78

5 Conclusion **79**

Bibliography **81**

List of Tables

2.1 Summary of calorimeter subsystem acronyms. 23
2.2 Summary of calorimeter system construction (*naph means PMMA acrylic doped with 8% naphthalene). 25
2.3 Energy resolution and η coverage of calorimeter systems. . . . 26
2.4 Coverage of calorimeter systems. *when there are two entries they are hadronic and em segmentation, respectively. 26
2.5 Geometry and η coverage of BSC. *Counters 2, 3, and 4 are square, the numbers in parentheses represent the value at the corner of the square counter. 28

3.1 Details of DIFF_DIPHOTON trigger cuts. † Denotes the cut is central only. 32
3.2 Details of electron candidate cuts (energy units are GeV). . . . 33
3.3 Summary of exclusivity cuts 36
3.4 Number of two-candidate events remaining after each exclusive cut. 36
3.5 Details of 16 signal events. *Angle is the 3-D opening angle of the electrons momenta. 40
3.6 Tight electron cuts 47
3.7 Summary of electron efficiencies 51
3.8 Summary of background numbers put into the cross section calculation. 65
3.9 Summary of numbers put into the cross section calculation. . 66

4.1 Details of central photon ID cuts (energy units are GeV). . . . 68
4.2 Conversion Cuts. 68
4.3 Details of 3 signal events. *Angle is the 3-D opening angle of the photons momenta. 69
4.4 Number of ExHuME MC events with both photons in $|\eta| < 1$ passing exclusive cuts (sequential). †MP and BSC are not yet simulated in cdfSim. 74
4.5 Summary of backgrounds 78
4.6 Summary of numbers put into the cross section calculation. † is from version 2 of exclusive e^+e^- note (CDF 7930) 78

List of Figures

1.1 The particles of the Standard Model organized into quarks, leptons, and bosons (the Higgs is not shown because it has not yet been experimentally verified) 2
1.2 a) represents the t-channel leading order process, b) represents the s-channel leading order process, c) represents one of the second order processes. The time axis goes from left to right. . 3
1.3 a) leptonic charged current exchange b) charged current flavor changing quark exchange c) neutral current exchange 4
1.4 a) s-channel gluon exchange between two quarks b) three gluon vertex is allowed because gluons carry colour c) 2^{nd} order exchange of gluons between quarks - this diagram is the basis of QCD mediated exclusive interactions because it allows the incoming and outgoing quarks to carry the same colour. 5
1.5 Exclusive interactions mediated by a) QCD and b) QED forming a central system, X. The grey areas represent interactions that are not completely specified by the diagram. 7
1.6 Two-photon processes to e^+e^- pairs; a) elastic-elastic process (also called exclusive) b)elastic-inelastic process c) inelastic-inelastic process. The p* and $\bar{p}$* represent excited states of the proton which quickly dissociate. 9
1.7 Durham model of QCD mediated exclusive interactions implemented in the ExHuME MC. The dashed line shows the factorization between the gluon luminosity and hard subprocess $gg \rightarrow X$. 11
1.8 a) dijet, b) χ_c, c) $\gamma\gamma$ gluon fusion processes 15

2.1 Fermilab accelerator chain 17
2.2 Basic concepts of particle detection. The layers represent the different detector systems of CDF. 18
2.3 The CDF detector. 20
2.4 CDF quarter section 21
2.5 Quarter section of calorimeters, showing projective tower geometry. 22
2.6 A central calorimeter wedge showing CHA, CEM, CPR, and CES. 23
2.7 A schematic of a CES chamber. 24
2.8 A schematic r-z view of the MP calorimeter. 27

2.9 A schematic of the CLC. Dotted lines represent high efficiency for particles from the interaction point and low efficiency for background. 28
2.10 A block diagram of the L1 and L2 trigger systems. 30

3.1 Trigger rate as a function of instantaneous luminosity for the DIFF_DIPHOTON trigger (trigger table PHYSICS_3_0[0-2] bit #37). 33
3.2 Log10(ADC counts - pedestal) in BSC-1 for interaction and non-interaction samples, the line shows the cut at 300 counts. Left plots are east, right plots are west. 35
3.3 Log10(ADC counts - pedestal) in BSC-2 for interaction and non-interaction samples, the line shows the cut at 300 counts. Left plots are east, right plots are west. 35
3.4 Log10(ADC counts - pedestal) in BSC-3 for interaction and non-interaction samples, the line shows the cut at 400 counts. Left plots are east, right plots are west. 37
3.5 Log10(Max Et) hit in mini-plug for interaction and non-interaction samples, the line shows the 5 MeV cut. Left plots are east, right plots are west. 37
3.6 Log10(Max Et) tower in the forward-plug region for interaction and non-interaction samples, the line shows the 30 MeV cut. Left is east, right is west. 37
3.7 Log10(Max Et) tower in the mid-plug region for interaction and non-interaction samples, the line shows the 80 MeV cut. Left is east, right is west. 38
3.8 Log10(Max Et) EM tower in the end-wall region for interaction and non-interaction samples, the line shows the 80 MeV cut. Left is east, right is west. 38
3.9 Log10(Max Et) HAD tower in the end-wall region for interaction and non-interaction samples, the line shows the 200 MeV cut. Left is east, right is west. 38
3.10 Log10(Max Et) tower in the central region for interaction and non-interaction samples, the line shows the 80 MeV and 200 MeV cuts for EM and Hadronic sections. Left is EM, right is Hadronic. 39
3.11 E_T of electrons in signal sample (points) compared to LPAIR MC (line) 40
3.12 eta (left) and phi (right) of electrons in signal sample (points) compared to LPAIR MC (line) 41
3.13 Delta ϕ (left) and invariant mass (right) of ee pairs in signal sample (points) compared to LPAIR MC (line) 41
3.14 p_z and p_T of ee pairs in signal sample (points) compared to LPAIR MC (line) 41

3.15 E_T of leading electron vs E_T of second electron (left) and 3-D opening angle of ee pairs in signal sample (points) compared to LPAIR MC (line) (right) 42
3.16 Event display of run 195762 event 3788. Note that there is no activity in the calorimeter or COT, other than the two electrons, and that both electrons originate from the beam line. 42
3.17 Electron reconstruction efficiency, $\varepsilon_{ee,rec}$, as a function of generator electron E_T . The grey line shows the 5 GeV cut. . . . 44
3.18 Electron reconstruction efficiency, $\varepsilon_{ee,rec}$, as a function of generator electron η and ϕ 45
3.19 Tight + Loose (ie. probe) electron invariant mass which shows a very clean J/Ψ peak. 46
3.20 Efficiency of the electron ID cuts (Had/Em plus CES shape). 47
3.21 Electron trigger efficiency, $\varepsilon_{e,trig}$, as a function of off-line E_T . 49
3.22 Electron trigger efficiency, $\varepsilon_{e,trig}$, as a function of off-line η and ϕ 49
3.23 The overall electron trigger efficiency, $\varepsilon_{e,trig}$, is calculated as the integral of the closed histogram divided by the integral of the open histogram. 50
3.24 Tracking efficiency. 51
3.25 LPAIR η distribution (empty histogram) and the LPAIR η distribution weighted by the tracking efficiency in that η bin (filled histogram). 52
3.26 EM time of electron 1 vs. electron 2 for non-cosmic events are plotted. Bin -99 corresponds to events with no EM timing information available. 53
3.27 Exclusive efficiency as a function of bunch luminosity. The fit curve is only a guide, it is not used to calculate the effective luminosity. The slope and intercept calculation shown indicate the level of inefficiency; if the cuts were perfect the intercept would be 1.0 and the cross section would be 60mb. The higher σ indicates that the cuts are conservative. 56
3.28 The n-1 efficiency as a function of instantaneous luminosity for each of the exclusive cuts. 56
3.29 $\mathscr{L}_{bunch}$ distribution for all zerobias data (open histogram with scale on left), ε_{exc} (points with scale on right), and weighted $\mathscr{L}_{bunch} \times \varepsilon_{exc}$ (filled histogram with scale on left) for calculation of ε_{exc}=0.0856 58
3.30 Jet fake rate (F_{jet}) is <2% 59
3.31 The cosmic background fraction is estimated to be 2.3×10^{-4}. There are more cosmic ray events with time greater than zero because the gate of the timing system is not symmetric around the bunch crossing time so clusters with high negative values are not recorded. 61

3.32 Number of associated towers for LPAIR MC, Z→ee data, and the electron sample (with no BSC cuts applied). LPAIR MC is normalized to events below 5 towers, Z→ee data is normalized to the events above 5 towers. 62
3.33 Number of associated towers for LPAIR MC, Drell-Yan MC, and the electron sample. LPAIR MC is normalized to events below 5 towers, Drell-Yan MC is normalized to the events above 5 towers. 63
3.34 The fraction of proton dissociations whose fragments would all remain in region greater than the η cut. 64
3.35 Plots show the number of events with a hit (ADC counts>400) in a PMT, given that there was (empty histogram) or was not (filled histogram) a hit in the adjacent PMT. The efficiency is the fraction of events in the empty histogram above 400 counts divided by the number of events in the empty histogram. . . . 65

4.1 E_T of photons in signal sample (points) compared to ExHuME MC (line) 69
4.2 η (left) and ϕ (right) of photons in signal sample (points) compared to ExHuME MC (line) 69
4.3 $\Delta\phi$ (left) and invariant mass (right) of photon pairs in signal sample (points) compared to ExHuME MC (line) 70
4.4 p_z and p_T of photon pairs in signal sample (points) compared to ExHuME MC (line) 70
4.5 E_T vs E_T (left) and 3d opening angle of photon pairs in signal sample (points) compared to ExHuME MC (line) 70
4.6 Event display of run 191089 event 127812. Note that there is no activity in the tracking chamber, and the only activity in the calorimeter is the two electromagnetic clusters. 71
4.7 Event display of run 199189 event 6276945. Note that there is no activity in the tracking chamber, and the only activity in the calorimeter is the two electromagnetic clusters. 71
4.8 Event display of run 200284 event 346775. Note the tracks consistent with a conversion in the tracking chamber, and the only activity in the calorimeter is the two electromagnetic clusters. 72
4.9 Event display of run 2000056 event 12978584 (not part of signal sample). 73
4.10 Jet fake rate (F_{jet}) is <3% before CES method correction, 1.8% after. 75
4.11 Number of associated towers in two-candidate events after tracking cut is applied. 76
4.12 Event display of run 206669 event 3531258. This is the single background event in Figure 4.11, and looks like a $\gamma\gamma$ event with a soft interaction (exactly what the exclusivity cut is designed to eliminate). 77

List of Symbols

Acronyms

ADC	Amplitude to Digital Converter
ATLAS	A Torodial LHC Apparatus
CDF	Run II Collider Detector Facility
EM	Electromagnetic
HAD	Hadronic
HERA	*ep* collider facility at DESY
ISR	Intersecting Storage Rings
FPT	Forward Proton Tagger
FP420	R&D Project to install FPTs at LHC
LHC	Large Hadron Collider
MC	Monte Carlo
MSSM	Minimally Supersymmetric Standard Model
PMT	Photomultiplier Tube
S$p\bar{p}$S	Super proton-antiproton Synchrotron
SM	Standard Model
SUSY	Supersymmetry
TDC	Time to Digital Converter
QCD	Quantum Chromodynamics
QED	Quantum Electrodynamics

CDF Detector Acronyms

BSC	Beam Shower Counters
CDFSOFT2	CDF off-line software package
CEM	Central Electormagnetic Calorimeter
CES	Central Electormagnetic Shower Max Detector
CESχ^2	χ^2 of cluster fit to expected CES shape
CHA	Central Hadronic Calorimeter
CLC	Cherenkov Luminosity Monitor
COT	Central Outer Tracker
CPR	Central Pre-Radiator Detector
Had/Em	Ratio of HAD to EM energy in cluster
Iso	Isolation energy of cluster
MP	Miniplug Calorimeter
PEM	Plug Electromagnetic Calorimeter
PHA	Plug Hadronic Calorimeter
SMX	Shower Max Detector (ie. CES)
L1,L2,L3	Level 1, 2 or 3 Trigger System
WHA	End-Wall Hadronic Calorimeter

Symbols

σ	Cross section
ε	Efficiency
α	QED coupling constant
α_s	QCD coupling constant
$D_\circ$	Distance of closest approach to beam line
ϕ	polar angle in CDF geometry
θ	azimuthal angle in CDF geometry
η	$-ln\tan(\frac{\theta}{2})$
E_T	$E\sin\theta$
p_T	$\lvert\vec{p}\rvert\sin\theta$
$\mathscr{L}$	Luminosity

Chapter 1

Theory and Motivation

This thesis contains the first observation of exclusive QED mediated e^+e^- production in hadron-hadron collisions, as well as the first evidence of QCD mediated exclusive $\gamma\gamma$ production in hadron-hadron collisions. The final results are presented in the form of a cross section measurement, significance of each observation, and a comparison to theoretical predictions. This first chapter is a brief introduction to the Standard Model of particle physics. It define what an exclusive interaction is, explains the mechanisms responsible for exclusive interactions within the Standard Model, and discusses how exclusive interactions could extend the physics reach of the experiments at the Large Hadron Collider (LHC).

1.1 The Standard Model

The Standard Model (SM) [1] is a description of the current understanding of the fundamental constituents of matter and their interactions. The constituents of matter are called as fermions (possessing half integer spin), while the particles responsible for their interactions are called bosons (possessing integer spin). The fermions are subdivided into quarks and leptons. Each class is represented in Figure 1.1 (the Higgs Boson is not shown because it has not yet been directly observed). Every fermion has an antimatter partner possessing the same mass and spin, but opposite charge and internal quantum numbers. The fermions can be divided into three generations, each generation containing more massive fermions than the previous generation (except for

the neutrinos, whose mass hierarchy has not be determined). The interactions between the fermions and bosons can be split into three related quantum field theories, quantum electrodynamics, electroweak theory, and quantum chromodynamics. Each theory will be discussed briefly in the following sections. Emphasis is placed on the concepts that are important for understanding the experimental measurements of this thesis.

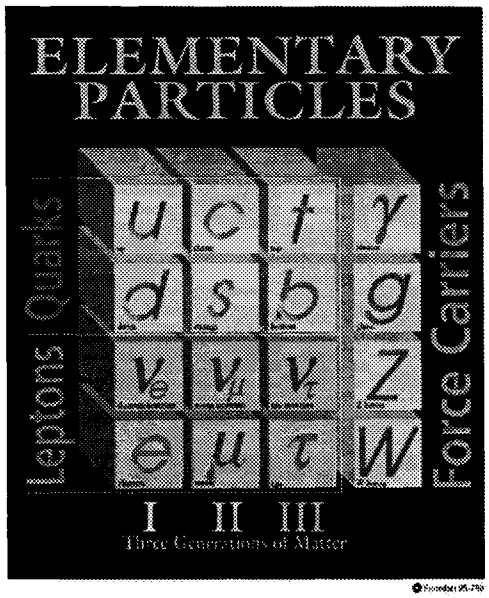

Figure 1.1: The particles of the Standard Model organized into quarks, leptons, and bosons (the Higgs is not shown because it has not yet been experimentally verified)

1.1.1 Quantum Electrodynamics

Quantum electrodynamics (QED) [2] is the theory governing the interactions between charged fermions and the photon. Interactions between fundamental particles are represented by Feynman diagrams. Three Feynman diagrams representing electron-positron scattering are shown in Figure 1.2. Since the initial and final states of all three interactions are identical, they must all contribute to the physical reality of electron scattering, and hence their amplitudes must be summed in a calculation of the interaction's properties. Figures 1.2a and 1.2b are the leading order (containing the smallest number of vertices possi-

ble) diagrams for electron scattering , while 1.2c is a second order diagram (containing the second smallest number of vertices possible). There are an infinite number of higher order (more than two vertices) diagrams that must be summed to calculate the observable properties of the interaction. Each vertex contributes a factor of $\alpha \sim \frac{1}{137}$, so the higher the order of the diagram the lower its contribution is to the observable properties. It is a perturbative expansion about α. Using Feynman diagrams and the corresponding summing rules defined by Feynman in the 1940's, all electromagnetic interactions can be completely described. This is QED. The Feynman calculus was developed in the context of QED, but is applicable to electroweak theory and some regions of quantum chromodynamics as well.

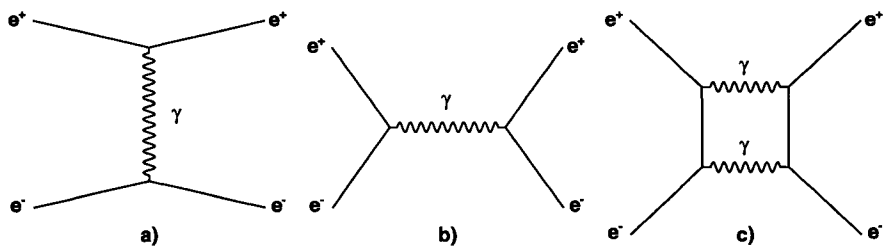

Figure 1.2: a) represents the t-channel leading order process, b) represents the s-channel leading order process, c) represents one of the second order processes. The time axis goes from left to right.

1.1.2 Electroweak Theory

The $W^{\pm}$ and Z° bosons are the mediators of the weak force and can interact with any fermion [3]. In charged current interactions the charged leptons ($e^{\pm}$,$\mu^{\pm}$,$\tau^{\pm}$) are converted to their corresponding neutrinos (ν_e,ν_μ,ν_τ) by the emission of a $W^{\pm}$. Charged current interactions in the quark sector are similar, charge $+\frac{2}{3}$ quarks (u,c,t) are converted to charge $-\frac{1}{3}$ quarks (d,s,b) by the emission of a W^{+}, but here the conversion does not have to stay in the same generation. The coupling of each quark flavor to every other quark flavor is defined in the 3x3 CKM matrix. Neutral current interactions (mediated by the Z°) leave the interacting fermion's species unchanged.

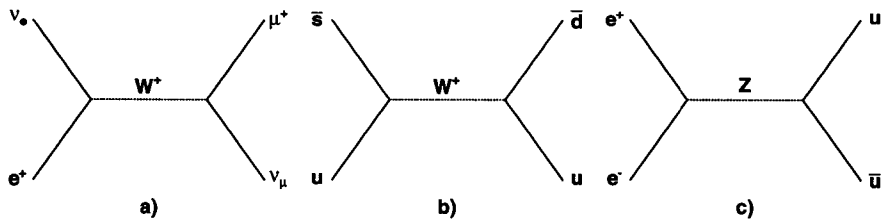

Figure 1.3: a) leptonic charged current exchange b) charged current flavor changing quark exchange c) neutral current exchange

1.1.3 Quantum Chromodynamics

Quantum chromodynamics [4] (QCD) is the theory describing the strong force. The strong force is mediated by the gluon which only interacts with quarks. Figure 1.4 shows some QCD interactions of quarks and gluons. The charge of the strong force is called colour and comes in three varieties; red, green, and blue.

There is a major difference between QED and QCD that leads to very observable effects - the gluons carry colour charge, while the photon is electrically neutral. This leads to gluons coupling directly to other gluons, forming three and four gluon vertices, which leads to the fact that the QCD coupling constant, α_s, is not a constant at all[1]. α_s is a *running* coupling constant, it depends on the separation distance (or momentum transfer, q) between the interacting quarks. At large q (short distance) α_s is small, while at small q (long distance) α_s is large. This is called *asymptotic freedom.*

In the region where $\alpha_s \ll 1$ the perturbative Feynman calculus can be applied, hence this region is called perturbative QCD. In the region where $\alpha_s \sim 1$, higher order diagrams contribute more and more to the calculation, so the perturbative expansion is no longer useful. This is called the non-perturbative region of QCD. There is not yet an analytical solution for interactions in the non-perturbative region, so theorists depend on phenomenological models and calculations that approximate space-time as a discrete latice to predict physical

[1]Actually, α isn't really constant either, but it changes very little in the currently accessible energy regime

results in this regime.

The most observable consequence of the running of α_s is called *confinement*. The mechanism of confinement has not yet been analytically proven because it depends on non-perturbative QCD. Confinement is the experimental observation that coloured particles are always bound together in colourless combinations. This can be conceptually understood by considering a $q\bar{q}$ pair being pulled apart. As the distance between them increases, the potential energy increases (because α_s is increasing), and eventually there will be enough potential energy to create another $q\bar{q}$ pair. Therefore the attempt to pull a quark from a bound state results in two (or more) bound states rather than a free quark. A bound state of quarks is called a *hadron*. Hadrons that contain two quarks ($q\bar{q}$ pairs) are called *mesons*, while hadrons that contain three quarks (qqq or $\bar{q}\bar{q}\bar{q}$) are called *baryons*. While not yet definitively observered by experiment, the bound state of two or more gluons, called a *glueball*, is possible.

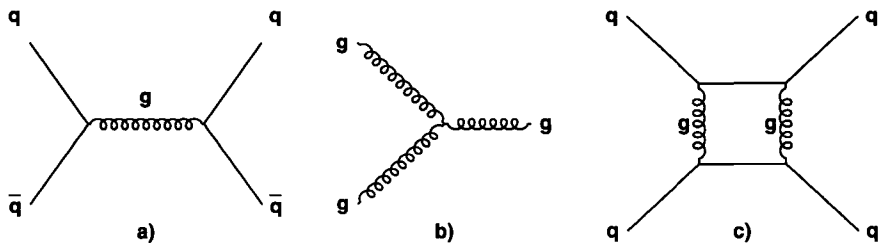

Figure 1.4: a) s-channel gluon exchange between two quarks b) three gluon vertex is allowed because gluons carry colour c) 2^{nd} order exchange of gluons between quarks - this diagram is the basis of QCD mediated exclusive interactions because it allows the incoming and outgoing quarks to carry the same colour.

1.1.4 The Higgs Boson

The Higgs Boson is the only particle of the Standard Model that has not yet been experimentally observed [1]. Analogous to the electric charge defining a particle's coupling to the photon field in QED and the colour charge defining the quark (or gluon) coupling to the gluon field in QCD, the mass of a particle

defines its coupling to the Higgs field. Just as the photon is the physical manifestation of the photon field, and the gluon is the physical manifestation of the strong field, the Higgs Boson is the physical manifestation of the Higgs field.

The Standard Model does not predict the mass of the Higgs, but it does predict that it is a scalar [5]. By starting with the Klein-Gordon Lagrangian for a complex scalar field, ϕ, adding a potential term of the form $-\frac{1}{2}\mu^2\phi^2 + \frac{1}{4}\lambda^2\phi^4$, and then writing the Lagrangian in a carefully chosen gauge, the new Lagrangian describes the Feynman rules for the interactions of the $W^{\pm}$, Z°, γ, and Higgs bosons with the fermions. The $W^{\pm}$, Z°, and Higgs bosons are predicted to be massive, while the γ is predicted to be massless. The choice of the Klein-Gordon Lagrangian as a starting point is what defines the SM Higgs as a scalar. Choosing a spin-$\frac{1}{2}$ or spin-1 Lagrangian to start from would result in a vacuum that is not rotationally invariant and would not result in the prediction of the experimentally observed $W^{\pm}$, Z°, and γ bosons.

Searches for Higgs at the Large Electron Positron (LEP) collider have excluded Higgs masses below 114.4 GeV/c^2 (95% CL) [6], while fits to electroweak parameters (top quark and $W^{\pm}$ masses) indicate that the Higgs mass is less than 175 GeV/c^2 (95% CL) [7]. The experimental confirmation or rejection of the Standard Model Higgs is one of the primary objectives of the LHC.

1.1.5 Beyond the Standard Model

The Standard Model is not a complete description of nature, there are many fundamental questions it does not answer including the hierarchy problem, Dark matter, and quantum gravity. A widely accepted potential solution to many of these questions is an extension to the Standard Model called *supersymmetry*. The basic concept of supersymmetry is that every boson in the Standard Model has a fermionic super-partner, and likewise, every fermion has a bosonic super-partner. If SUSY were an exact symmetry the particles and their super-partners would have the same mass, therefore SUSY is a broken symmetry. The search for evidence of supersymmetry is another objective

of the LHC.

That concludes this very brief introduction to the Standard Model. The remainder of this chapter is devoted to explaining what exclusive interactions are and why they are interesting.

1.2 Exclusive Interactions

An exclusive interaction is defined in this thesis as an inelastic hadron-hadron interaction in which the hadrons do not dissociate; they escape the interaction intact. The hadrons of interest in this thesis are protons and antiprotons, which are equivalent in this context. Therefore, 'proton',p, will be used to describe either particle. Exclusive interactions, $pp \rightarrow p + X + p$, can be mediated by QED or QCD, as shown in Figure 1.5. The central system, X, is completely reconstructed in the experimental observation. The use of the terms 'QED' and 'QCD' mediated interactions is motivated by the coupling to the proton - gluons in the case of QCD mediated, and photons in the case of QED mediated.

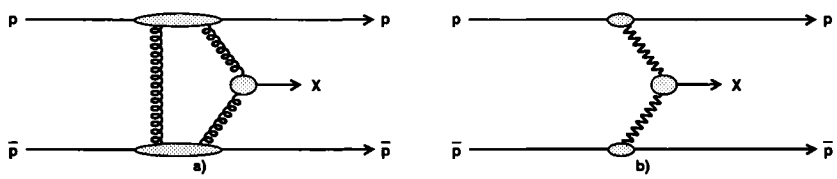

Figure 1.5: Exclusive interactions mediated by a) QCD and b) QED forming a central system, X. The grey areas represent interactions that are not completely specified by the diagram.

This thesis reports the search for both QED mediated interactions with an e^+e^- central system, and QCD mediated interactions with a $\gamma\gamma$ central system ($gg \rightarrow \gamma\gamma$ through a quark loop). While these interactions may seem different from a theoretical perspective (QED vs. QCD), they have almost identical, yet easily distinguishable, experimental signatures. Photons and electrons produce the same signal in the electromagnetic calorimeter, but only electrons produce a track in the tracking chamber, see Chapter 2. The similarity in the

detector signatures means that many parts of the analysis are shared, while easily distinguishable means they can be experimentally separated.

Another advantage comes from the fact that the QED mechanism is theoretically well known and has a reasonably high cross section. The QCD mechanism is not as well understood theoretically, and the cross section is ~10 times smaller. The similarity between the detector signatures means that the measurement of the QED process can be used to significantly increase the confidence in the QCD measurement. A firm observation of the QED process that matches the theoretical predictions means that the detector and backgrounds are well understood for the QCD measurement.

1.2.1 QED Mediated Exclusive Interactions

QED mediated exclusive interactions are a subset of a class of interactions referred to in most *ee* collider literature as 'two-photon' processes[8, 9, 10], in most heavy ion literature as 'ultra-peripheral' interactions[11, 12], and in *ep* collider literature as 'electroproduction' [13, 14]. In this thesis, all of these processes are called QED mediated interactions, defined as the production of a central system through a t-channel photon exchange in lepton-lepton, lepton-hadron, or hadron-hadron interactions. In an *exclusive* QED mediated interaction, the central system is completely reconstructed and the incident hadrons do not dissociate.

Exclusive QED mediated interactions have never been observed in hadron-hadron collisions. The cross section would be too low for observation at the Intersecting Storage Ring (ISR)[2] or the Super Proton Antiproton Synchrotron ($Sp\bar{p}S$)[3]. The Axial Field Spectrometer experiment at ISR observed ~100k exclusive $\pi^+\pi^-$ events with a cross section of 30 μb [15]. Using the LPAIR Monte Carlo (MC) program [16, 17], the cross section for the QED mediated exclusive e^+e^- cross section in the same kinematic region at the exclusive $\pi^+\pi^-$ is ~100 pb at $\sqrt{s} = 63$ GeV. Using this estimate, one would only have expected 0.3 exclusive e^+e^- events. The integrated luminosity at the $Sp\bar{p}S$

[2]The ISR was a pp collider with $\sqrt{s} = 63$ GeV that ran at CERN from 1971 to 1984
[3]The $Sp\bar{p}S$ was a $p\bar{p}$ collider with $\sqrt{s} = 400$ GeV that ran at CERN from 1981 to 1989

was even lower than the ISR (because it used $\bar{p}$'s), so observation there would have been even less likely and so no search was made.

This thesis outlines the observation of exclusive QED mediated production of e^+e^- pairs in proton-proton collisions, as shown in Figure 1.6. Figure 1.6a is the diagram for QED mediated exclusive interactions, 1.6b and 1.6c are closely related processes where one or both protons are excited and then dissociate (denoted by the $p*$). The diagrams in 1.6b and 1.6c are not considered to be exclusive processes.

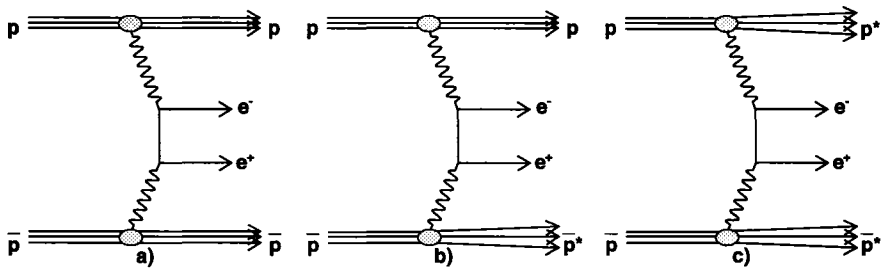

Figure 1.6: Two-photon processes to e^+e^- pairs; a) elastic-elastic process (also called exclusive) b)elastic-inelastic process c) inelastic-inelastic process. The p* and $\bar{p}$* represent excited states of the proton which quickly dissociate.

The only portion of the diagrams in Figure 1.6 that is not exactly calculable with the Feynman rules are the grey regions representing the proton structure function. The proton is a composite particle, so the proton structure function is used in place of a quark-photon vertex.

The LPAIR MC program [16, 17] simulates all three processes in Figure 1.6. It has been shown to agree with HERA data [18], so there is confidence that it should correctly simulate Tevatron data. LPAIR MC is used as the signal MC for the exclusive e^+e^- analysis.

1.2.2 QCD Mediated Exclusive Interactions

The Durham model [19, 20, 21, 22] is the most highly developed and widely accepted theoretical calculation describing QCD mediated exclusive interactions. The Durham group are the only group to provide a prediction for exclusive $\gamma\gamma$ production, thus it will be used as a theoretical comparison in

this thesis. The Durham calculation replaces the protons in Figure 1.5a with quarks and uses perturbative QCD to determine a cross section, see Figure 1.7. The model then replaces the gluon-quark vertices with an estimation of the hadronic matrix element that represents the coupling of two gluons to a proton. This produces the desired cross section, with the exception of two factors; 1) the probability that the gluons in the hard subprocess will radiate, making the interaction not exclusive; and 2) the probability that there is another soft interaction, independent of the diagram just calculated, that will make the interaction not exclusive. The application of a Sudakov form factor [23] ensures the exclusive final state is not spoiled by emission off the hard subprocess. However, the probability that there is no other soft interaction lies in the realm of non-perturbative QCD, and is therefore not calculable (at this time). This is called the "soft survival factor" or the "gap survival probability", S^2, and is estimated by the Durham group to be 0.045 at Tevatron energies and 0.03 at LHC energies. The estimate of S^2 is a fits to ISR, $Sp\bar{p}S$, Tevatron, and HERA data. The soft survival factor is one of the largest sources of uncertainty in the Durham model; the other is the low-x gluon uncertainty. The hard subprocess $gg \to X$ is factorizable, so it can be replaced with the colour singlet, spin zero, projection of any matrix element calculation of gg-fusion. In the exclusive $\gamma\gamma$ case the hard subprocess is $gg \to \gamma\gamma$.

In the limit where the outgoing quarks carry no tranverse momentum, the z-component of angular momentum of central system vanishes. Outgoing quarks carrying very small transverse momentum correspond to the outgoing protons scatter through a small angle. Since such a small amount of the incoming proton's longitudinal momentum is lost (typically only $\sim$1%), small angle scatter is a very good approximation. The result is that the central system will have J_z=0. If the protons do not dissociate, then charge conjugation and parity must be restricted to $C = +1$ and $P = +1$. These restrictions are called the spin selection rule, $J_z^{PC} = 0^{++}$. The Durham model is implemented in the matrix element MC generator called ExHuME[24]. ExHuME is used as the signal MC for the $\gamma\gamma$ analysis. It is the only MC generator that simulates exclusive $\gamma\gamma$ production.

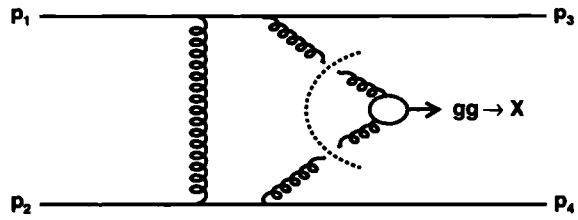

Figure 1.7: Durham model of QCD mediated exclusive interactions implemented in the ExHuME MC. The dashed line shows the factorization between the gluon luminosity and hard subprocess $gg \to X$.

An alternative language for the coupling of a colourless combination of gluons the Pomeron. The Pomeron comes from the phenomenological study of diffraction, derived from Regge theory [25]. Regge theory is the study of the scattering amplitudes of hadronic states. The Pomeron is phenomenological object responsible for the exchange of any state with the vacuum quantum numbers.

There has been one other observation of an exclusive QCD mediated interaction, $\pi^+\pi^-$ production at the ISR [15]. While this measurement shows that exclusive QCD mediated interactions are possible, it is not very useful for comparing to predictions at the LHC because the center of mass energy ($\sqrt{s}$=63 GeV) was so much lower than the LHC and the $\pi^+\pi^-$ invariant mass was small (< 3 GeV/c^2).

1.3 Why are Exclusive Interactions Interesting?

Exclusive interactions can assist in the search for and measurement of new physics at the LHC. QCD and QED mediated exclusive interactions yeild slightly different benefits. The QCD mediated interactions benefit from two important properties:

1. *Missing Mass:* The mass of the central system, M_X, can be determined by measuring the momentum of the outgoing protons, $M_x^2 = (p_1 + p_2 - p_1' - p_2')^2$ [26].

by measuring the momentum of the outgoing protons,
$M_x^2 = (p_1 + p_2 - p_1' - p_2')^2$ [27].

2. *Spin Selection Rule:* In QCD mediated exclusive interactions, X is preferentially produced with the quantum numbers of the vacuum, $J^{PC} = 0^{++}$.

In the search for the SM Higgs, the cross section for the QCD mediated exclusive Higgs $pp \rightarrow p + H + p$ was calculated by the Durham group to be 3 fb for $M_H = 120$ GeV/c^2, falling to 1 fb at $M_H = 200$ GeV/c^2 with an uncertainty of a factor of three [19]. While this low cross section means that exclusive interactions are unlikely to be a discovery channel for the SM Higgs, there are several ways that the exclusive Higgs interaction can be used at the LHC [28].

- Using the missing mass, the Higgs mass can be measured to a resolution of $\sim$2 GeV/c^2 [29], a better resolution than any other light Higgs channel.
- If the Higgs width is greater than 3 GeV/c^2 and the mass is greater than 165 GeV/c^2, then the width can be measured with the missing mass.
- Due to the spin selection rule, an observation of an exclusive Higgs will also be a measurement of the Higgs quantum numbers, something that no other currently proposed channel can accomplish.
- Also due to this spin selection rule, the QCD $b\bar{b}$ ($q\bar{q}$) background is greatly reduced, allowing the H $\rightarrow b\bar{b}$ branching ratio to be measured.
- It provides another Higgs search channel with a 3σ signal prediction for a 120 GeV/c^2 Higgs in only 30 fb^{-1} [29]

In Beyond the SM physics there is such a wide variety of models and scenerios that it is not reasonable to discuss each one. One advantage that exclusive interactions have is the ability to search for resonances in the missing mass spectrum. Even if the resonance decayed to an unobservable final state, the mass could be measured with the missing mass.

There are some models that have been widely studied that have particular regions of phase space that will not be well covered by inclusive mesurements, but could be covered by using exclusive interactions. A few examples are:

- In the 'intense coupling' region of the minimal super-symmetric standard model (MSSM), the two scalar Higgs bosons (h,H) will have a signal to background ratio above 20 (for Higgs masses around 130 GeV/c^2). This is an increase in the signal to background ratio by an order of magnitude over the inclusive channels in this region of the MSSM. Also, h and H might be close in mass and could possibly be distinguished by the missing mass. [22]

- The CPX scenario, a model with an explicit CP-violating Higgs, predicts very light Higgs bosons masses (less than 60 GeV/c^2) which would have evaded LEP searches. Central exclusive production provides a larger cross section for light CPX Higgs than conventional channels. [30]

QED mediated exclusive interactions are not constrained by the spin selection rule, but they have very well known cross sections. Because the cross sections are so well known, the QED mediated processes $pp \rightarrow p + \mu^+\mu^- + p$ can be used as a tool for luminosity monitoring [26]. Using the missing mass of the outgoing proton the QED mediated exclusive interactions can also be used in searches for and measurement of new physics that couple to photons.

Exploiting exclusive interactions at the LHC requires that the outgoing protons are measured. The FP420 project is a research and development project aimed at installing Forward Proton Taggers (FPT) at both ATLAS and CMS [31]. The FPTs would be capable of measuring the momenta of the outgoing protons, making the identification of exclusive interactions possible in an environment with many inelastic $p\bar{p}$ interactions per bunch crossing (pile-up). If these detectors are installed, exclusive interactions will be able to assist in the search for, and measurement of, the SM Higgs Boson and physics Beyond the SM at the LHC.

A major challenge for the FP420 project is the fact that (until now) there have been no direct tests of the theoretical models used to make predictions

Central State	Advantages	Disadvantages
Dijet	high cross section	difficult to determine "exclusivity"
χ_c	experimentally clean	pQCD calculation is questionable
Diphoton	experimentally clean	low cross section

of exclusive interactions at the LHC. The motivation for this thesis is to test the theoretical models for QED and QCD mediated exclusive interactions. A confirmation of the predicted cross sections will mean that one can put more confidence in the models which means a higher probability that FPTs will be installed and the benefits of exclusive interactions can be exploited in the search for new physics at the LHC.

1.4 Other Related Work at CDF

This thesis is concerned exclusive e^+e^- and $\gamma\gamma$ interactions, but there are several other exclusive final states being studied at CDF. In the QED sector, exclusive production of muon pairs is being studied. Because low momentum ($\sim$1.5 GeV/c^2) muons can be experimentally identified with greater certainty than electrons, the muon channel will likely be the only useful exclusive channel for luminosity monitoring at the LHC. Its observation at CDF will be an important test of the experimental challenges that would be faced in attempting to extract an exclusive signal in the presence of pile-up.

In the QCD mediated exclusive inteactions there are three exclusive final states that have been identified as valuable tests and are potentially measurable at the Tevatron: dijets, χ_c, and $\gamma\gamma$. The hard subprocesses of these are shown in Figure 1.8. The advantages and disadvantages of each process are listed in Table 1.4. The Durham group [20] say that the measurement of the exclusive diphoton cross section at the Tevatron could be a "standard candle" for exclusive theoretical predictions because it does not suffer from non-perturbative QCD calculation uncertainties and is a non-hadronic final state. The search for exclusive $\gamma\gamma$ production at CDF was first proposed in Ref. [32]

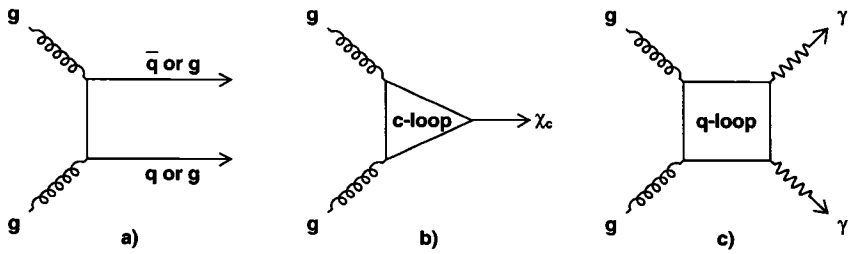

Figure 1.8: a) dijet, b) χ_c, c) $\gamma\gamma$ gluon fusion processes

1.5 Outline of Analysis Procedure

The measurement of a cross section is really just a counting experiment. A cross section is a measure of the probability of some final state occuring given some initial state. The initial state is a proton and an antiproton with equal (980 GeV/c) and opposite momenta. The final state is a proton and antiproton with slightly less than 980 GeV/c plus the central state. The central states considered in this thesis are e^+e^- (with E_T >5 GeV and $|\eta| < 2$) and $\gamma\gamma$ (with E_T >5 GeV and $|\eta| < 1$).

The central state is observed in the CDF detector, but the proton and antiproton go undetected because CDF does not have detectors capable of observing them in the kinematic region of this analysis. The protons are assumed to have stayed intact if no particles (other than the central state) are observed in the detector. The cross section is then calculated using:

$$\sigma = \frac{N_{signal} - N_{background}}{\varepsilon_i \int \mathscr{L}} \tag{1.1}$$

Where N_{signal} is the number of events that are consistant with the signal, $N_{background}$ is an estimate of the number of N_{signal} events that are not truly signal, ε_i are the efficiencies for detecting signal events, and $\int \mathscr{L}$ is the integrated luminosity.

Chapter 2

Accelerator and Detector

The Fermilab accelerator complex is a chain of accelerators starting from a bottle of hydrogen and ending in proton-antiproton collisions at center of mass energy ($\sqrt{s}$) of 1.96 TeV in the 5000-ton CDF[1] and DZero detectors. This chapter will describe the Fermilab accelerator complex, as well as the components of the CDF detector that are relevant to this analysis. An exhaustive description of the CDF detector can be found in the CDF Technical Design Report [33]

2.1 Accelerator Complex

The proton acceleration chain begins with hydrogen gas in the Cockcroft-Walton pre-accelerator, Figure 2.1.[2] The hydrogen gas is ionized to create H^- ions and accelerate them to 750 keV. The ions are then sent to a 150 m long linear accelerator (Linac) which accelerates the ions to 400 MeV. The ions are then sent through a carbon foil, where the electrons are stripped off, leaving just the protons being sent into the Booster. The Booster is a circular accelerator, accelerating the protons to 8 GeV, before sending them to the Main Injector.

In the Main Injector the 8 GeV protons can either be accelerated to 150 GeV and injected into the Tevatron, or they can be accelerated to 120 GeV and sent into the Target Hall. In the Target Hall the protons collide with a

[1] CDF stands for the Run II Collider Detector Facility

[2] The Proton, Neutrino, and Meson beam lines pictured are not significant to this thesis.

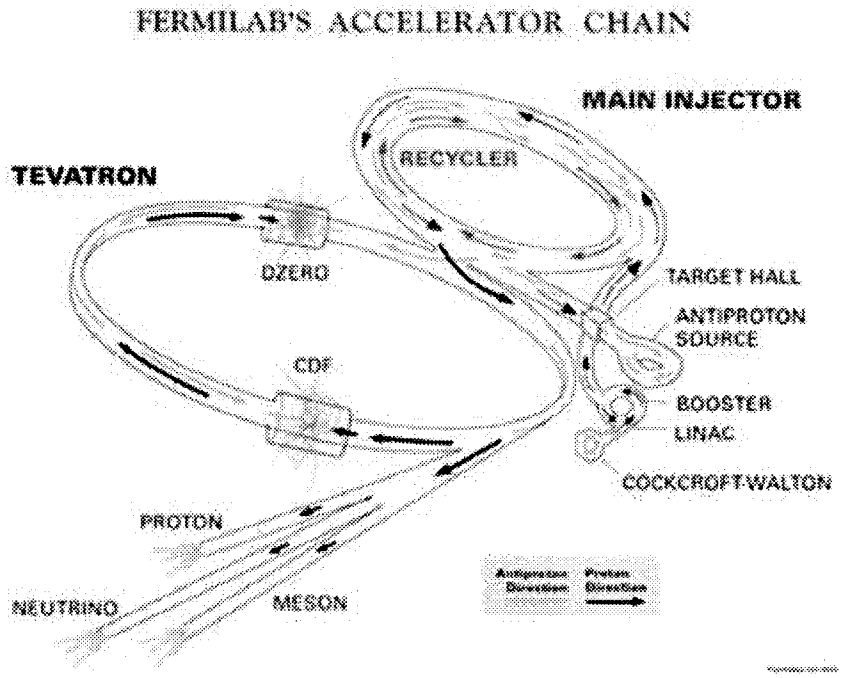

Figure 2.1: Fermilab accelerator chain

nickel target and produce antiprotons that are collected in the antiproton Source. When a sufficient number of antiprotons have been produced they are sent from the antiproton source to the Main Injector, where they are accelerated to 150 GeV and then injected into the Tevatron.

Once injected into the Tevatron the protons and antiprotons are accelerated together from 150 GeV to 980 GeV. The protons and antiprotons circulate in opposite directions in the Tevatron in bunches. There are 36 bunches of protons and 36 bunches of antiprotons circulating in the Tevatron. At a luminosity $\sim 100 \times 10^{30}\text{cm}^{-2}\text{s}^{-1}$, there are $\sim 100 \times 10^{10}$ protons per bunch and about an order of magnitude fewer antiprotons per bunch. The bunches are arranged in 3 trains of 12 bunches each, with 2.2 μs separating each train. There are 396 ns separating each bunch within the train. This produces a maximum bunch crossing rate of 2.5 MHz and a mean bunch crossing rate of 1.7 MHz. The bunches are brought into collision in the center of the CDF and DZero detectors.

2.2 CDF Detector

The CDF detector is a multipurpose particle detector originally constructed for the Tevatron Run I, then upgraded for the Tevatron Run II. First data for the CDF Run II detector was taken in June 2001. The goal of the detector is to identify the characteristics of the final products of $p\bar{p}$ collisions at the center of the detector, the *interaction point.* The basic principles of particle detection are shown in Figure 2.2.

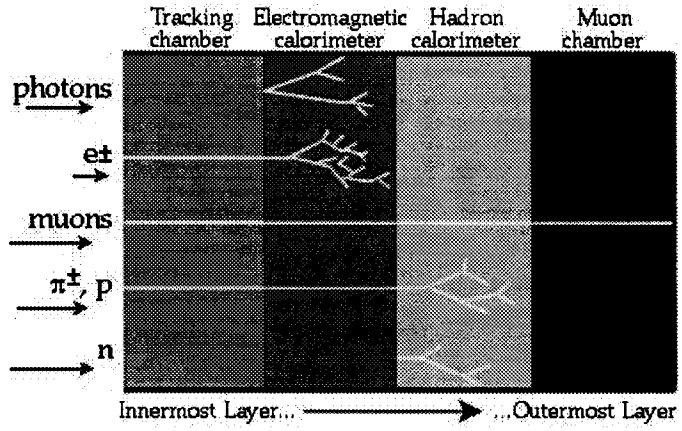

Figure 2.2: Basic concepts of particle detection. The layers represent the different detector systems of CDF.

Uncharged particles do not leave a signal in the tracking chambers. Photons and electrons shower (deposit their energy) in the electromagnetic calorimeter, while hadrons shower in the hadronic calorimeter. Muons are the only particles that traverse the entire detector to leave a signal in the outermost muon chambers. Using these basic properties photons, electrons, muons, charged and neutral hadrons are distinguished from one another. Based on these properties of particle detection, the CDF detector is made up of three fundamental sections: tracking detectors, calorimeters, and muon detectors. These three systems are composed of many subsystems; those used in this analysis will be explained in detail.

CDF uses a right handed coordinate system with its origin at the center of the detector, which is also the nominal interaction point of the $p\bar{p}$ colli-

sions. The positive $\hat{z}$-axis points in the direction of the proton beam (west to east), the positive $\hat{y}$-axis points upward, and the positive $\hat{x}$-axis points radially outward in the plane of the Tevatron ring. CDF has a cylindrical shape, so cylindrical coordinates are more convenient to use. The radial distance, r, is defined as the distance from the $\hat{z}$-axis, ϕ is the azimuthal angle, and θ is the polar angle.

Variables commonly used in particle physics include the rapidity, $y = \frac{1}{2}ln(\frac{E+p_z}{E-p_z})$, and the pseudorapidity, $\eta = -ln\tan(\frac{\theta}{2})$. Also used are transverse energy, $E_T = E\sin\theta$ and transverse momentum, $p_T = |\vec{p}|\sin\theta$. Another useful quantity is the angular separation between two objects, defined as $R = \sqrt{\Delta\eta^2 + \Delta\phi^2}$

Figure 2.3 shows a cutout view of the CDF detector, while Figure 2.4 shows a more detailed quarter-section view with detector components labeled. The different η regions of the detector are described as central ($|\eta| < 1$), plug ($1 < |\eta| < 3$), and forward ($3 < |\eta| < 7$). The remainder of this chapter is devoted to the detailed description of the relevant components of the CDF detector.

2.2.1 Tracking Detectors

The tracking detectors are located inside a 1.4 T magnetic field pointing along the -$\hat{z}$-direction. The field is created by a 4.8 m long, 3 m diameter, superconducting solenoid. The magnetic field allows a charged particle's p_T to be determined by measuring the radius of curvature of the track. The tracking detectors include the silicon detectors and the Central Outer Tracker.

Silicon Detector

The CDF silicon detector is composed of three subsystems; Layer00 (L00), the Silicon Vertex Detector (SVXII), and the Intermediate Silicon Layer (ISL). All three systems use the same basic principle of silicon strip detectors - when a charged particle passes through the depletion region of a biased p-n semiconductor junction it creates electron-hole pairs which can be detected as electrical signals on a strip. The silicon detectors are not required in this analysis. A

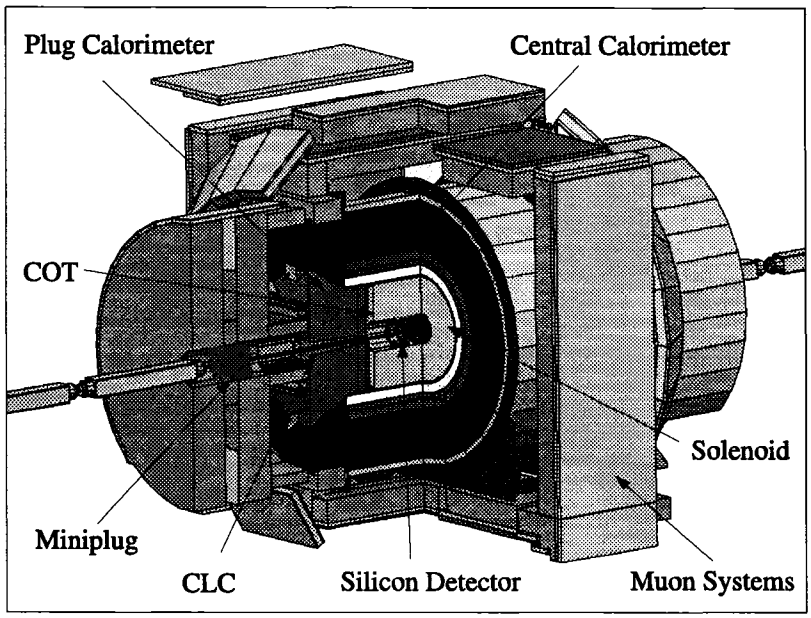

Figure 2.3: The CDF detector.

more detailed description of them can be found in [33]

L00 Layer00 is a radiation hard single-sided layer located on the outer surface of the beam pipe ($r \approx 1.5cm$).

SVXII The Silicon Vertex Detector has five layers of double-sided silicon placed between r of 1.5 and 11 cm.

ISL The Intermediate Silicon Layer consists of one or two (depending on η) layers of double sided silicon placed with r between 22 and 29 cm.

Central Outer Tracker

The Central Outer Tracker (COT) is a 3m long cylindrically shaped drift chamber extending between 40 < r < 132 cm. The COT has full coverage in the central ($|\eta| < 1$) region, and partial coverage in the forward region ($1 < |\eta| < 2$). It contains 8 'super-layers' each with 12 layers of sense wires interleaved with potential wires. Even-numbered layers are axial (parallel to the beam line), while odd-numbered layers are stereo ($\pm 2°$ from parallel to

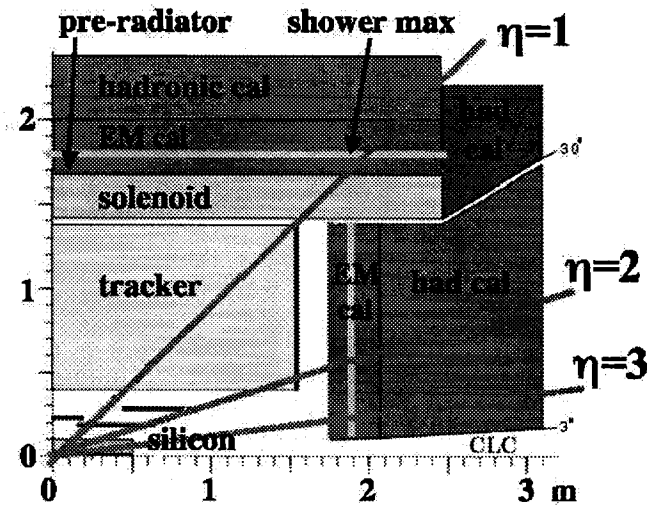

Figure 2.4: CDF quarter section

beam line). The COT is filled with a mixture of argon and ethane with small amounts of alcohol and oxygen. This gas mixture ionizes as a charged particle passes through it, leaving a trail of ions that drift toward the sense wires in the fields created by the potential wires. The ions avalanche close to the sense wire, producing a measurable electrical signal which is sent to the readout systems. A charged particle passing radially through the COT will give 96 measurements to which a track can be fit.

2.2.2 Calorimeters

All of the CDF calorimeters are scintillator sampling calorimeters. A sampling calorimeter alternates layers of an absorber material, like lead, with an active material, like scintillator. As a particle passes through the absorber layers it showers and deposits large amounts of energy, while as it passes through the active material the energy of the shower is sampled. The total amount of energy read out of all the sampling layers is proportional to the energy of the incident particle(s). The CDF calorimeter system is split into electromagnetic and hadronic parts to provide rudimentary particle identification, as shown in Figure 2.2.

The CDF calorimeter system is composed of ten subsystems, listed in Table 2.1 with the function of the subsystem. The location of each subsystem is shown in Figure 2.5.

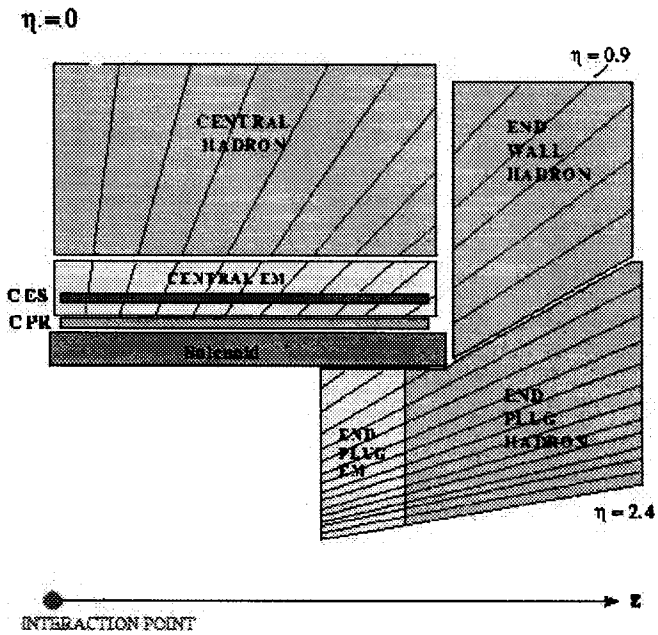

Figure 2.5: Quarter section of calorimeters, showing projective tower geometry.

Central Calorimeters (CHA,WHA,CEM)

The central calorimeter is a cylindrical shaped detector filling r from 1.5m to 3.0m and z from -2.5m to 2.5m. It covers the region from $30° < \theta < 150°$ and 2π in azimuth. The CEM and CHA are contained in the same mechanical support structure, called a wedge. There are 24 central wedges on each (east and west) side of the detector. The WHA is also divided into 24 wedges on each side. Each wedge covers 15° in azimuth, a central wedge is shown in Figure 2.6. The central wedges are combined with the endwall wedges and segmented into 12 towers per side, as shown in Figure 2.5. This makes a total of 1152 EM towers and 1152 hadronic towers in the central calorimeter. Each tower covers 15° in azimuth and 0.11 units in η. The towers are arranged in a projective geometry, meaning that they all point back to the interaction

Calorimeter Subsystems	
Acronym	Name
CHA	Central Hadronic Calorimeter
WHA	End-Wall Hadronic Calorimeter
CEM	Central Electromagnetic Calorimeter
CES	Central Electromagnetic Shower Max Detector
CPR	Central Pre-Radiator Detector
PHA	Plug Hadronic Calorimeter
PEM	Plug Electromagnetic Calorimeter
PPR	Plug Pre-Radiator Detector
MP	Miniplug Calorimeter

Table 2.1: Summary of calorimeter subsystem acronyms.

point. The details of the materials used can be found in Table 2.2, while the resolution and η coverage can be found in Table 2.3

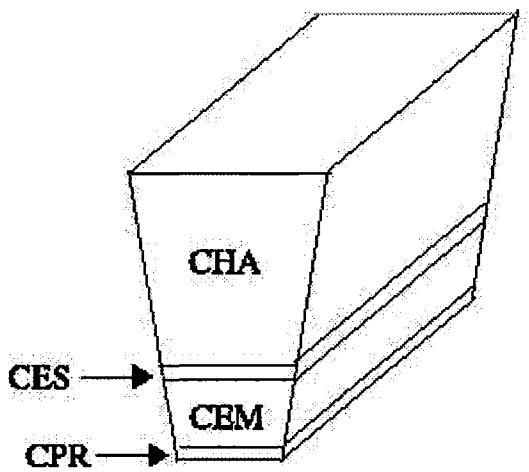

Figure 2.6: A central calorimeter wedge showing CHA, CEM, CPR, and CES.

CES and CPR

When searching for photons in an event, it is difficult to distinguish between photons from the primary interaction and photons that are the daughters of π° decay. When a π° is highly boosted, the two photons will be almost

collinear. The CES and CPR use different methods to distinguish between a single photon and a pair of photons from π° decay.

The CES is a proportional chamber (Argon, CO_2 gas mixture) located $5.9X_o$ (including solenoid) into the CEM, see Figure 2.6. The CES uses signals from the 'wires' and 'strips' to determine the position and lateral profile of an EM shower, see Figure 2.7. To determine if a hit in the CEM is a single photon or two nearly collinear photons, the lateral profile of the EM shower is compared to a profile determined in test beam using a χ^2 test.

The CES provides position resolution (± 2 mm) of an EM shower in an CEM tower, which significantly helps distinguish one or two EM showers below 35 GeV (typical width of an EM shower is $\sim$1 cm). Above 35 GeV the photons from π° decay are too close together for the CES to distinguish them efficiently.

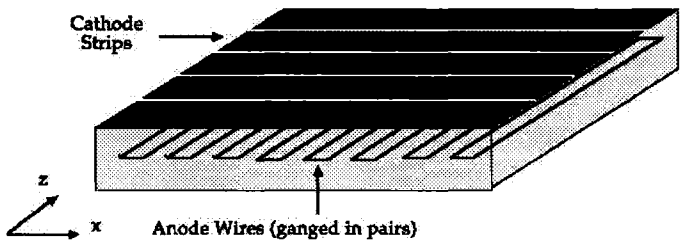

Figure 2.7: A schematic of a CES chamber.

Instead of using the physical separation of two photons, the CPR uses the fact that two photons will be more likely to create an EM shower than a single photon when traversing through the solenoid. The CPR is a layer of scintillator tiles located between the solenoid and the CEM. The CPR will register a hit if a photon has converted (into an e^+e^- pair) in the solenoid, but will not register a hit if the photon did not convert. The solenoid is about $1X_o$ deep (depending slightly on θ), so the probability for one photon to convert is 72%. The probability that at least one photon from a π° decay will convert is 92%. So an EM shower with a CPR hit is more likely to be from a π° decay than a single photon. This method is only statistical, it cannot be used for

Calorimeter Construction				
System	# Layers	Absorber (cm)	Scintillator (cm)	Depth
CEM	30	Pb (0.3)	SNSC38 (0.5)	$18X_o, 1\lambda_o$
CHA	32	Fe (2.5)	naph* (1.0)	$4.7\lambda_o$
WHA	15	Fe (5.0)	naph* (1.0)	$4.7\lambda_o$
PEM	23	Pb (0.5)	SNSC38 (0.4)	$23X_o, 1\lambda_o$
PHA	23	Fe (2.5)	SNSC38 (0.6)	$7\lambda_o$
MP	36	Pb (0.5)	Bicron517L (0.6)	$32X_o$, $1.3\lambda_o$

Table 2.2: Summary of calorimeter system construction (*naph means PMMA acrylic doped with 8% naphthalene).

a single event but can help determine the fraction of π^0's in a sample of EM showers above 35 GeV, where the CES method becomes inefficient.

Plug Calorimeter (PHA, PEM, PPR)

The plug region has analogous components to the central calorimeter system; electromagnetic (PEM) and hadronic (PHA) calorimeters, and a pre-radiator detector (PPR). It covers the polar region from 3° to 37° ($1.1 < |\eta| < 3.6$), with 2π azimuthal coverage. The towers have a projective geometry with segmentation ($\Delta\theta \times \Delta\eta$) ranging from $7.5° \times 0.1$ to $15° \times 0.6$. Energy resolution and details of construction can be found in Tables 2.2 and 2.3

Miniplug Calorimeter

The Miniplug calorimeter (MP) is a small cylindrical calorimeter placed at z = 580cm to 640cm and r = 6cm to 33cm, see Figure 2.8. Due to the high radiation in this forward region the scintillation material chosen was a liquid scintillator, rather than an acrylic. This allowed the calorimeter to be designed with a 'towerless' geometry, meaning that there are no physical barriers between light collection sites. Light collection is done via 336 wavelength shifting fibers that run to multichannel PMTs. To accomodate data collection, bundles of 4 fibers are read out together and called 'towers' - making 84 towers per side. Material and resolution details of the MP calorimeter are in Tables 2.2 and 2.3.

Calorimeter Resolution and Coverage		
System	$\sigma(E)/E$	η Coverage
CEM	$14\%/\sqrt{E_T}+2\%$	$\lvert\eta\rvert < 1$
CHA	$50\%/\sqrt{E_T}+5\%$	$\lvert\eta\rvert < 1$
WHA	$50\%/\sqrt{E_T}+5\%$	$0.7 < \lvert\eta\rvert < 1.3$
PEM	$16\%/\sqrt{E_T}+1\%$	$1.1 < \lvert\eta\rvert < 3.6$
PHA	$80\%/\sqrt{E_T}+5\%$	$1.1 < \lvert\eta\rvert < 3.6$
MP	$18\%/\sqrt{E_T}+1\%$	$3.6 < \lvert\eta\rvert < 5.2$

Table 2.3: Energy resolution and η coverage of calorimeter systems.

Calorimeter Coverage					
Tower	ieta(E, W)	System	$\Delta\eta$	$\Delta\theta$	$\Delta\phi^*$
0	25 26	CEM/CHA	0 - 0.11	90° - 82°	15°
1	24 27	CEM/CHA	0.11 - 0.22	82° - 75°	15°
2	23 28	CEM/CHA	0.22 - 0.33	75° - 68°	15°
3	22 29	CEM/CHA	0.33 - 0.44	68° - 62°	15°
4	21 30	CEM/CHA	0.44 - 0.55	62° - 57°	15°
5	20 31	CEM/CHA	0.55 - 0.66	57° - 52°	15°
6	19 32	CEM/CHA/WHA	0.66 - 0.77	52° - 46°	15°
7	18 33	CEM/CHA/WHA	0.77 - 0.88	46° - 43°	15°
8	17 34	CEM/CHA/WHA	0.88 - 0.99	43° - 40°	15°
9	16 35	CEM/WHA	0.99 - 1.10	40° - 37°	15°
10	15 36	PEM/CEM/WHA	1.10 - 1.20	37° - 33°	15° , 7.5°
11	14 37	PEM/PHA/WHA	1.20 - 1.32	33° - 30°	15° , 7.5°
12	13 38	PEM/PHA	1.32 - 1.41	30° - 27°	7.5°
13	12 39	PEM/PHA	1.41 - 1.52	27° - 25°	7.5°
14	11 40	PEM/PHA	1.52 - 1.64	25° - 22°	7.5°
15	10 41	PEM/PHA	1.64 - 1.78	22° - 19°	7.5°
16	9 42	PEM/PHA	1.78 - 1.93	19° - 16°	7.5°
17	8 43	PEM/PHA	1.93 - 2.11	16° - 14°	7.5°
18	7 44	PEM/PHA	2.11 - 2.33	14° - 11°	15°
19	6 45	PEM/PHA	2.33 - 2.61	11° - 8°	15°
20	5 46	PEM/PHA	2.61 - 3.00	8° - 6°	15°
21	4 47	PEM/PHA	3.00 - 3.64	6° - 3°	15°
22	3 48	MP	3.6 - 3.9	2.8° - 2.2°	n/a
23	2 49	MP	3.9 - 4.2	2.2° - 1.7°	n/a
24	1 50	MP	4.2 - 4.6	1.7° - 1.2°	n/a
25	0 51	MP	4.6 - 5.2	1.2° - 0.6°	n/a

Table 2.4: Coverage of calorimeter systems. *when there are two entries they are hadronic and em segmentation, respectively.

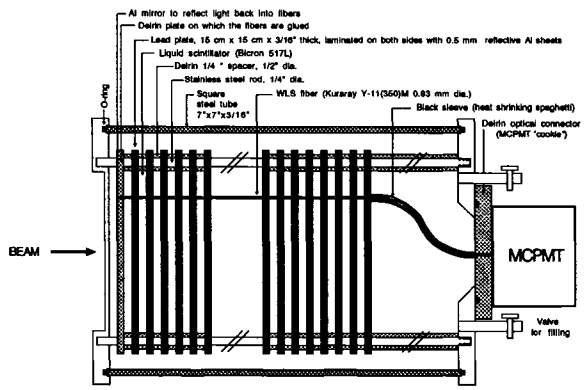

Figure 2.8: A schematic r-z view of the MP calorimeter.

2.2.3 Cherenkov Luminosity Counter

The Cherenkov Luminosity Counter (CLC) is used to measure the instantaneous and integrated luminosity of the $p\bar{p}$ beam in the CDF detector. The CLC is located in the space between the plug calorimeter and the beam line, see Figure 2.9. It is made of 48 aluminized mylar tubes (2m$\times$ $\sim$2cm) filled with isobutane gas pointing toward the interaction point. The tubular construction makes the CLC very efficient to particles coming from the interaction point, but inefficient for particles coming from beam background and secondary interactions. This means that the CLC can efficiently count the number of bunch crossings with at least one $p\bar{p}$ interaction. Using this and the inelastic cross-section for $p\bar{p}$ interactions the luminosity can be determined.

2.2.4 Beam Shower Counters

The Beam Shower Counters (BSC) are used to trigger on diffractive events. They are made of scintillator paddles (read out with acrylic light-guides) wrapped around the beam line. There are 4 counters on the west side and 3 counters on the east, their position, geometry, and η coverage is shown in Table 2.5.

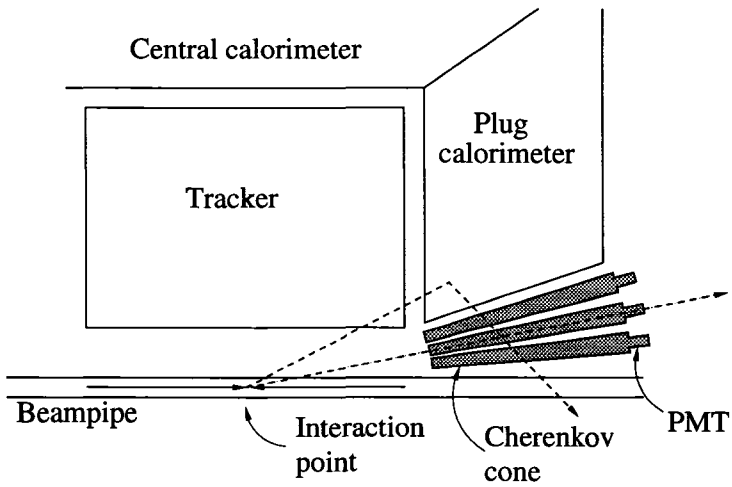

Figure 2.9: A schematic of the CLC. Dotted lines represent high efficiency for particles from the interaction point and low efficiency for background.

BSC Geometry and η Coverage*				
Counter	z (m)	Inner r (cm)	Outer r (cm)	η Coverage
BSC-1	±6.6	3.8	5.9	$5.4 < \|\eta\| < 5.9$
BSC-2	±23.2	3.8	7.6 (10.8)	$(6.1)6.4 < \|\eta\| < 7.1$
BSC-3	±31.6	3.8	7.6 (10.8)	$(6.4)6.7 < \|\eta\| < 7.4$
BSC-4	56.4	3.8	7.6 (10.8)	$(7.0)7.3 < \eta < 8.0$

Table 2.5: Geometry and η coverage of BSC. *Counters 2, 3, and 4 are square, the numbers in parentheses represent the value at the corner of the square counter.

2.2.5 Muon Chambers

For muons with energy below several hundred GeV, ionization is the dominant energy loss mechanism. This means that muons from Tevatron $p\bar{p}$ collisions act as minimum ionizing particles as they pass through the CDF detector. They pass through the calorimeters, leaving only a small amount of energy, and then pass through the muon chambers. The muon chambers are a set of drift chambers with steel absorber plates outside the calorimeters, see Figure 2.3. A muon is identified as a small track (stub) in the muon chambers matched to a track in the COT with only a small amount of energy deposited in the calorimeters in between.

2.2.6 Trigger

The collision rate at CDF is too high (2.5 MHz) to record every event. A selection process is required to choose physically interesting events as they occur in the detector. CDF has a three level trigger system, each level putting more stringent selection criteria on the event. It takes the 2.5 MHz bunch crossing rate down to 75 interesting events per second written to tape with only ~5% dead-time.

The Level-1 (L1) trigger takes the maximum bunch crossing rate of 2.5 MHz down to ~30 kHz using hardware specifically designed for CDF. Information from the calorimeters, COT, BSC, and muon systems are processed into L1 calorimeter, track, and muon objects, see Figure 2.10. To form a L1 calorimeter object, a 24×24 grid of trigger towers is formed by combining adjacent calorimeter towers into towers with 15° ×0.2 segmentation. The L1 calorimeter object is then defined as the EM or hadronic energy of the trigger tower. L1 track objects are 2-dimensional tracks ($p_T > 1.5$ GeV/c) made by tracing COT hits with the eXtremely Fast Tracker (XFT) and extrapolated to the silicon region with the eXtremely fast exTRaPolator (XTRP). L1 muon objects are composed of muon stubs from the muon chambers being matched to tracks from the XTRP. All these L1 objects are sent to the 'Global L1' processing, where they are combined with logical AND and OR gates to form L1 triggers. 'Global L1' has capacity for 64 different L1 triggers.

The Level-2 (L2) trigger is also made of custom built hardware and takes the ~30 kHz L1 rate and reduces it to ~350 Hz. Figure 2.10 shows the L2 decision is made with all the information from L1, plus information from the SVX and CES. L2 calorimeter objects use an elementary clustering algorithm. A cluster is defined as a contiguous region of L1 trigger towers with non-trivial energy. Each cluster begins with a tower above the *seed* threshold, then all towers above a shoulder threshold that form a contiguous region with the seed tower are added to the cluster. All L1 and L2 decisions are temporally coordinated with the Trigger System Interface and Clock (TSI/CLK).

The Level-3 (L3) trigger is a farm of ~500 CPUs in PCs running Scientific

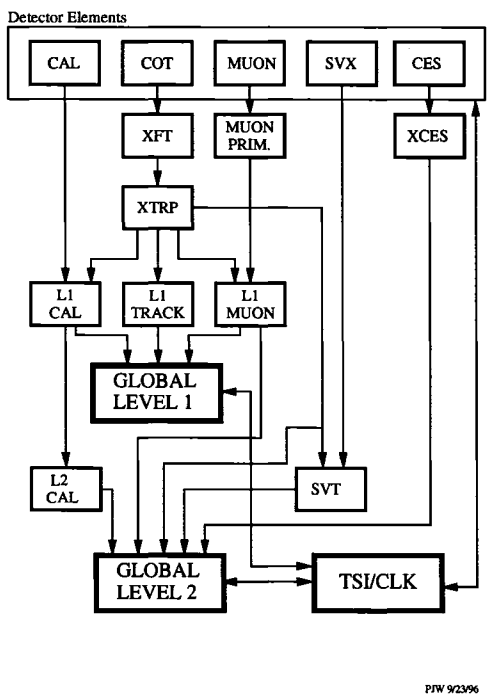

Figure 2.10: A block diagram of the L1 and L2 trigger systems.

Linux. It does a full event reconstruction for every event coming from L2. It takes roughly 1 second for a CPU to process one event. Having full event reconstruction at L3 means that event selection is very flexible and can be very specific with fully reconstructed tracks and jets. L3 takes the 350 Hz input from L2 and outputs events at 75 Hz. With a mean event size of ~200kB, that is a data rate of 15 MB/s being written to tape.

Chapter 3

Observation of Exclusive e^+e^- Production

This chapter contains a description of the first observation of QED mediated exclusive e^+e^- production via two-photon exchange in hadron-hadron collisions. The chapter begins by explaining the how 16 signal events were selected from 10^{12} $p\bar{p}$ collisions. The second section evaluates the efficiencies, and the third section estimates the backgrounds. Finally, in Section 3.4, the cross section is calculated and compared to the LPAIR MC prediction.

3.1 Event Selection

Selecting potentially interesting events from the 1.7 million bunch crossings per second is done with a trigger followed by a sequence of offline cuts. The offline cuts include electron ID (which identify electrons in the detector), exclusivity cuts (which check that there is no other observable particles in the detector), and cosmic cuts (which eliminate events triggered by cosmic rays).

3.1.1 Trigger and Good Run List

The trigger used for this analysis is called the DIFF_DIPHOTON trigger. This trigger was designed and installed in 2004 specifically for this analysis. The details of the trigger cuts are shown in Table 3.1. The trigger rate is very low and peaks at an instantaneous luminosity of about $20\times10^{30}\text{cm}^{-2}\text{s}^{-1}$, as shown in Figure 3.1. The peak in the trigger rate at $20\times10^{30}\text{cm}^{-2}\text{s}^{-1}$is expected

DIFF_DIPHOTON Trigger Details	
Level 1:	· BSC-1 Sum < 1000 ADC Counts (East and West) · 1 Plug or Central tower with: Had/Em<0.125 & E_T >4 GeV
Level 2:	· 2 Plug or Central towers with: Had/Em< 0.125 & E_T >4 GeV & $0 < \|\eta\| < 3.6$
Level 3:	· 2 EM clusters with: E_T >4 GeV & (Iso<2 GeV or IsoRatio<0.1) & CES $\chi^2 < 20.0^{\dagger}$

Table 3.1: Details of DIFF_DIPHOTON trigger cuts. † Denotes the cut is central only.

because multiple interactions spoil the rapidity gap requirement.

The trigger has been collecting data since December 7, 2004 in the low luminosity trigger tables "PHYSICS_3_*"[1]. The data used in the current analysis is the "gdif0h" dataset and part of the "gdif0i" dataset. This corresponds to runs 190697 to 206989 taken between December 7 2004 and November 9 2005. The dataset was produced with the CDFSOFT2 6.1.1 version of production and ntuplized into the dev_243 Stntuple with CDFSOFT2 6.1.2.

A good run list is applied to the dataset to eliminate runs in which a detector component was not functioning properly. The good run list used is a subset of the Data Quality Monitoring group's "version 11" list in which runs that were bad for SMX (CES Shower Max detector), MiniPlug, BSC were removed. Runs that used the high luminosity trigger tables and runs greater than 206989 were also excluded from the good run list. The total integrated luminosity for these runs is 532±32 pb^{-1}. The systematic uncertainty applied is 6%, which is the standard luminosity uncertainty at CDF.

3.1.2 Electron ID Cuts

The first step in the offline event selection is selecting electron candidates from the EM clusters in the triggered events. Since this analysis is being done in parallel with the search for exclusive $\gamma\gamma$ production, the initial cuts will pass both electrons and photons. The only measurable difference between photons

[1]The trigger was in for a short time from August 9-23 2004, runs 186081-186598 corresponding to 8.8 pb^{-1}which is not used in this analysis.

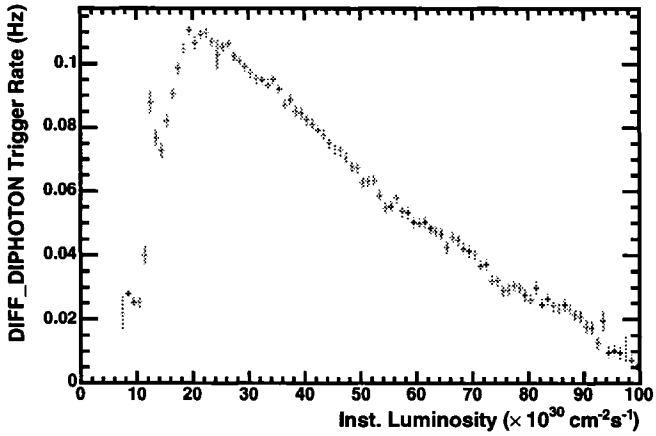

Figure 3.1: Trigger rate as a function of instantaneous luminosity for the DIFF_DIPHOTON trigger (trigger table PHYSICS_3_0[0-2] bit #37).

Cut	Central	Plug
Energy (GeV)	$E_t > 5.0$	$E_t > 5.0$
Shower Shape	CES χ^2 <20	PES χ^2 <10
Had/Em Ratio	Had/Em < 0.055 + 0.00045*E	Had/Em < 0.05

Table 3.2: Details of electron candidate cuts (energy units are GeV).

and electrons in the CDF detector is the presence of a track pointing to the electron's EM cluster. To keep the analyses equivalent for as long as possible, the track requirement will be applied in the last step of the analysis.

The ID cuts applied are shown in Table 3.2. They are based on the standard photon cuts recommended by the photon group. An EM object that passes the cuts in Table 3.2 will be called an *electron candidate*. The collection of all events with two electron candidates will be referred to as the *two-candidate sample*. The standard isolation cuts are not applied in this set of cuts because the exclusivity cuts are equivalent to isolation cuts. The exclusivity cuts are explained in Section 3.1.4.

3.1.3 Cosmic Cut

Cosmic rays arrive in the detector at random times. The EM calorimeter has a timing system (EM timing) that records the arrival time of the EM cluster relative to the beam crossing time. In order to remove cosmic rays from the data sample, the EM timing of each electron must be less than 10 ns, the difference between the EM timing of the two electrons is required to be less than 10 ns, and the electrons are required to be separated by more than 90° in ϕ. The $\Delta\phi$ separation cut also removes events triggered by beam halo. The efficiency and background of these cuts is discussed in Sections 3.2.3 and 3.3.2. While cuts on other variables could be applied, we choose to use only the EM timing and $\Delta\phi$ cuts because they can be used for both photon and electron samples.

3.1.4 Exclusivity Cuts

In order to determine if the event was exclusive, one must determine that there was nothing (other than the two EM objects) in the detector. In order to do that, you must know what "nothing" looks like in the detector. To accomplish this, two samples of events were made from zerobias[2] data, *interaction* and *non-interaction*. Events with no tracks (a track is defined as the default CDF track with p_T >200 MeV/c), no hits in the CLC (a CLC hit defined as any CLC tube having >150 ADC counts), and no muon stubs (a muon stub is a track in the muon detectors), were put into the non-interaction sample. All other zerobias events were put into the interaction sample. In the remainder of this section these samples will be used to motivate the exclusivity cuts on the BSC and calorimeters. Note that these track, CLC, and muon cuts are not being applied to the exclusive electron sample, they are only being use to help define appropriate calorimeter cuts that will be applied to the signal sample.

Figure 3.2 shows the maximum number of ADC counts in any of the BSC-1 PMTs for the interaction and non-interaction samples (one entry per event). It shows that 300 ADC counts distinguishes between an interaction and no

[2]Zerobias means that the events were recorded with no selection criteria other than the beam crossing time.

interaction in BSC-1. Note that the interaction events also have a peak < 300 ADC counts because not all interaction events have a particle passing through the BSC. The exclusivity cut on the BSC-1 is there set to 300 ADC counts, meaning that an event must have all BSC-1 channels less than 300 counts to be defined as exclusive. Figures 3.3 and 3.4 show the corresponding plots for BSC-2 and BSC-3. A cut of 400 counts is chosen for BSC-3 because the pedestal is slightly wider. Note that the BSC-2 and BSC-3 plots do not show a peak above the pedestal because their design differs from BSC-1.

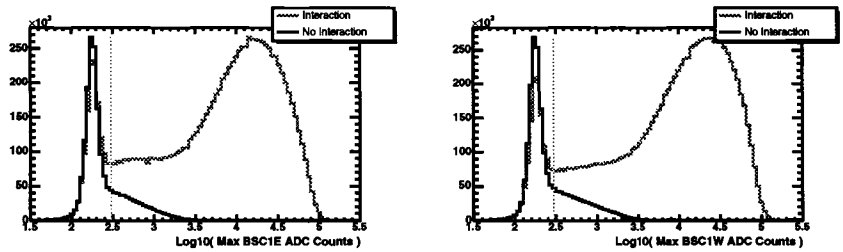

Figure 3.2: Log10(ADC counts - pedestal) in BSC-1 for interaction and non-interaction samples, the line shows the cut at 300 counts. Left plots are east, right plots are west.

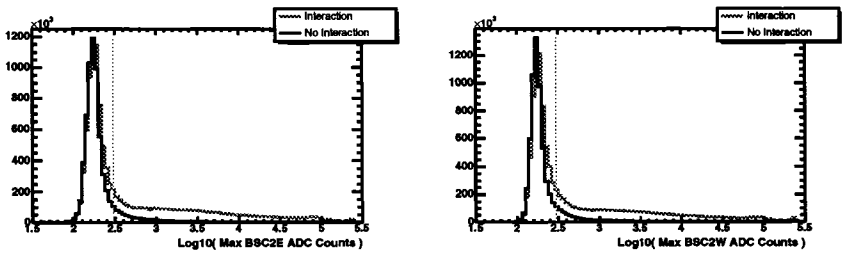

Figure 3.3: Log10(ADC counts - pedestal) in BSC-2 for interaction and non-interaction samples, the line shows the cut at 300 counts. Left plots are east, right plots are west.

The calorimeters are divided into five regions; mini-plug region (towers 22 to 25, $3.6 < |\eta| < 5.2$), the forward-plug region (towers 18 to 21, $2.11 < |\eta| < 3.64$), the mid-plug region (towers 12 to 17, $1.32 < |\eta| < 2.11$), the end-wall region (towers 6 to 11, $0.66 < |\eta| < 1.32$), and the central region (towers 0 to

Region	Towers	Eta Range	Cut
BSC-3	n/a	$6.7 < \|\eta\| < 7.4$	<400 ADC counts
BSC-2	n/a	$6.4 < \|\eta\| < 7.1$	<300 ADC counts
BSC-1	n/a	$5.4 < \|\eta\| < 5.9$	<300 ADC counts
MiniPlug	22 to 25	$3.6 < \|\eta\| < 5.2$	$E_T < 5$ MeV
Forward Plug	18 to 21	$2.11 < \|\eta\| < 3.64$	$E_T < 30$ MeV
Mid Plug	12 to 17	$1.32 < \|\eta\| < 2.11)$	$E_T < 80$ MeV
End Wall	6 to 11	$0.66 < \|\eta\| < 1.32$	EM $E_T < 80$ MeV, HAD $E_T < 200$ MeV
Central	0 to 5	$0.00 < \|\eta\| < 0.66$	EM $E_T < 80$ MeV, HAD $E_T < 200$ MeV

Table 3.3: Summary of exclusivity cuts

Sample	Number of Events
Pass All BSC	12433
Pass MiniPlug	489
Pass FwdPlug	95
Pass MidPlug	68
Pass EndWall	33
Pass Central	27

Table 3.4: Number of two-candidate events remaining after each exclusive cut.

5, $0.00 < |\eta| < 0.66$). Figures 3.5 to 3.10 show the highest E_T tower for the five regions in the interaction and non-interaction samples. The grey vertical lines in the plots show the energy threshold chosen for the cut in that region. The central and end-wall regions are divided into EM tower and HAD tower cuts due to the large difference in the noise levels of the two sections[3]. These plots motivate the cuts shown in Table 3.3.

The exclusivity cuts are applied to all towers in two-candidate sample events except for the electron towers. An electron tower is defined as any tower in the electron cluster plus any towers within one tower of the electron seed tower. The number of two-candidate events that pass each cut (in sequence from BSC to Central) is shown in Table 3.4.

[3]The calorimeter data has a default PMT spike killer for towers greater than 500 MeV. A spike killer routine requiring that both calorimeter PMTs fired is also applied to all towers below 500 MeV.

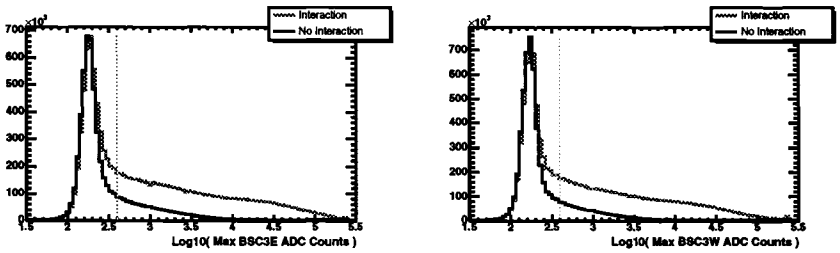

Figure 3.4: Log10(ADC counts - pedestal) in BSC-3 for interaction and non-interaction samples, the line shows the cut at 400 counts. Left plots are east, right plots are west.

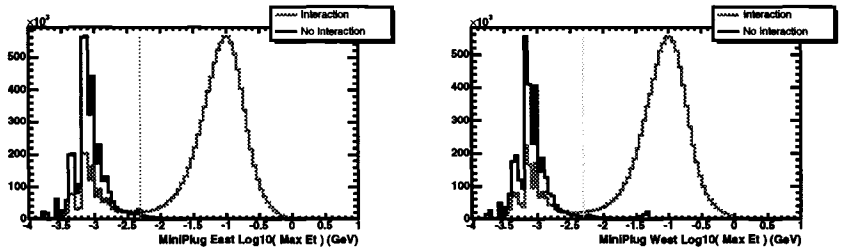

Figure 3.5: Log10(Max Et) hit in mini-plug for interaction and non-interaction samples, the line shows the 5 MeV cut. Left plots are east, right plots are west.

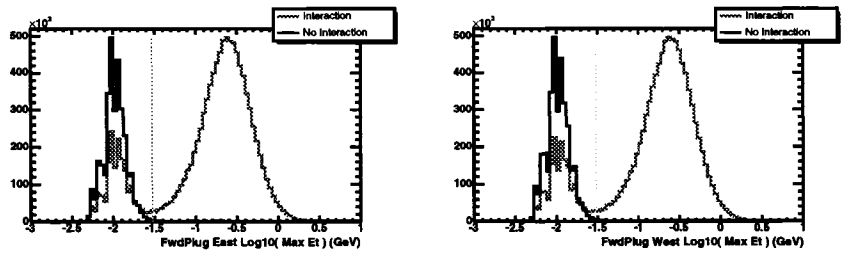

Figure 3.6: Log10(Max Et) tower in the forward-plug region for interaction and non-interaction samples, the line shows the 30 MeV cut. Left is east, right is west.

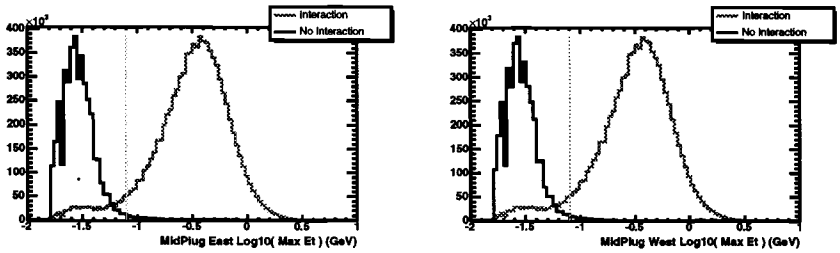

Figure 3.7: Log10(Max Et) tower in the mid-plug region for interaction and non-interaction samples, the line shows the 80 MeV cut. Left is east, right is west.

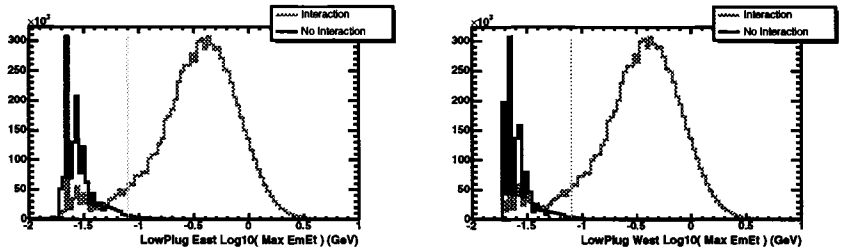

Figure 3.8: Log10(Max Et) EM tower in the end-wall region for interaction and non-interaction samples, the line shows the 80 MeV cut. Left is east, right is west.

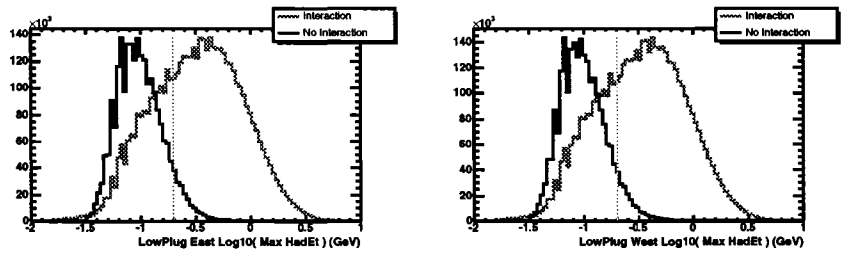

Figure 3.9: Log10(Max Et) HAD tower in the end-wall region for interaction and non-interaction samples, the line shows the 200 MeV cut. Left is east, right is west.

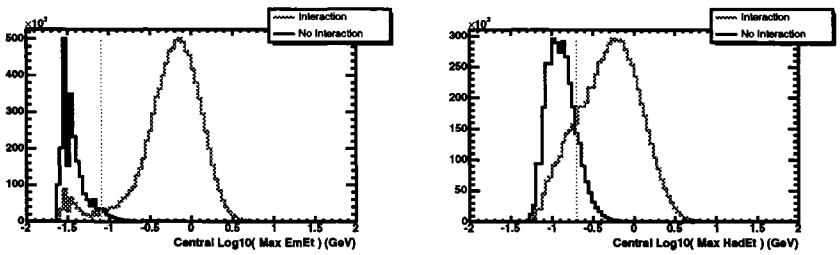

Figure 3.10: Log10(Max Et) tower in the central region for interaction and non-interaction samples, the line shows the 80 MeV and 200 MeV cuts for EM and Hadronic sections. Left is EM, right is Hadronic.

3.1.5 Track Cut

As shown in Table 3.4, 27 events from the two-candidate sample pass the exclusive cuts. To distinguish the electrons from photons, each electron candidate is required to have a single track with p_T >1 GeV/c pointing to its EM cluster. 16 events pass this cut. These events are called the *signal sample*, and are discussed in the following section.

3.1.6 Signal Sample

The details of the 16 signal sample events are given in Table 3.5 and compared to the LPAIR Monte Carlo in Figures 3.11 to 3.15 (normalized to unit area). They show that there is agreement between the data and MC within the statistics of the sample. Figures 3.16 shows an event display of a typical signal event.

Run	Event	E_T (GeV)	η	$\Delta\phi$	Angle*	M (GeV/c^2)
191425	284590	8.7, 8.5	-0.31, -0.55	3.13	2.3	17.4
191596	1594224	16.5, 9.0	-0.20, -0.32	3.14	2.7	24.4
195762	3788	15.2, 14.6	0.39, 0.14	3.11	2.6	30.0
196752	1657477	6.3, 6.2	0.81, 0.71	3.10	1.8	12.5
197657	13796201	8.4, 7.8	-0.47, -1.22	3.14	2.0	17.2
197763	7914309	7.5, 7.3	-0.35, 0.65	3.13	3.0	16.7
198514	14359480	6.1, 5.5	0.15, 0.92	3.10	2.2	12.3
200056	10189203	7.3, 6.7	0.79, 1.62	3.13	1.2	15.3
200570	4578964	5.7, 5.1	-0.72, -1.46	3.13	1.4	11.7
200719	7411538	6.5, 5.8	-0.00, 1.61	3.11	2.0	16.2
201155	151042	19.3, 18.8	0.33, 0.12	3.14	2.7	38.4
201371	1580716	5.3, 5.0	0.82, 1.29	3.13	1.4	10.6
202771	18236977	8.2, 7.5	0.25, -1.22	3.12	2.4	20.1
203153	12396961	6.8, 6.4	1.49, 0.10	3.14	1.9	16.4
204119	2569312	6.0, 5.0	-0.42, -1.05	3.14	1.6	11.2
205894	1786515	12.7, 11.2	0.65, -0.97	3.14	2.9	31.9

Table 3.5: Details of 16 signal events. *Angle is the 3-D opening angle of the electrons momenta.

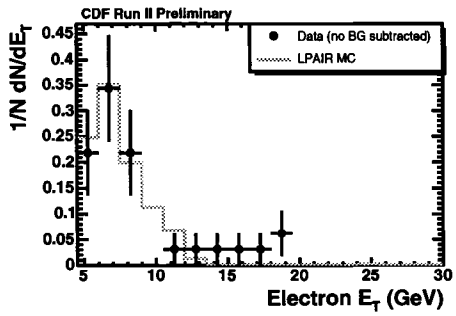

Figure 3.11: E_T of electrons in signal sample (points) compared to LPAIR MC (line)

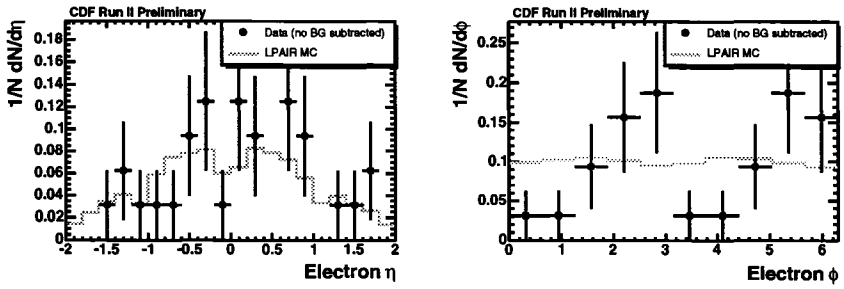

Figure 3.12: eta (left) and phi (right) of electrons in signal sample (points) compared to LPAIR MC (line)

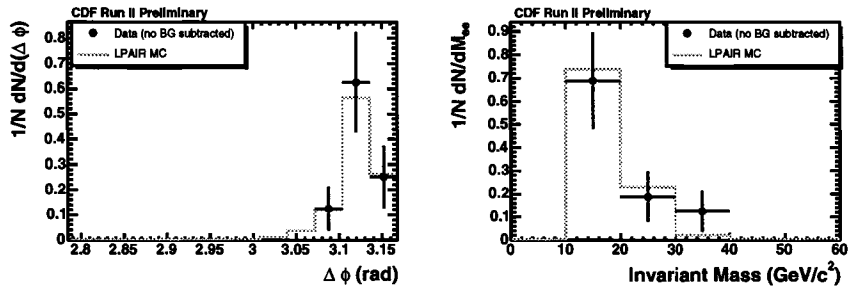

Figure 3.13: Delta ϕ (left) and invariant mass (right) of ee pairs in signal sample (points) compared to LPAIR MC (line)

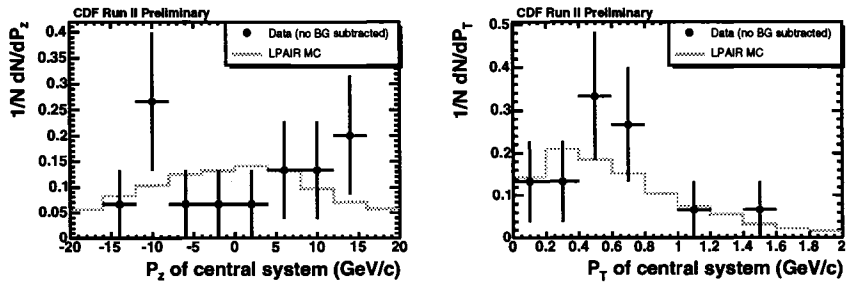

Figure 3.14: p_z and p_T of ee pairs in signal sample (points) compared to LPAIR MC (line)

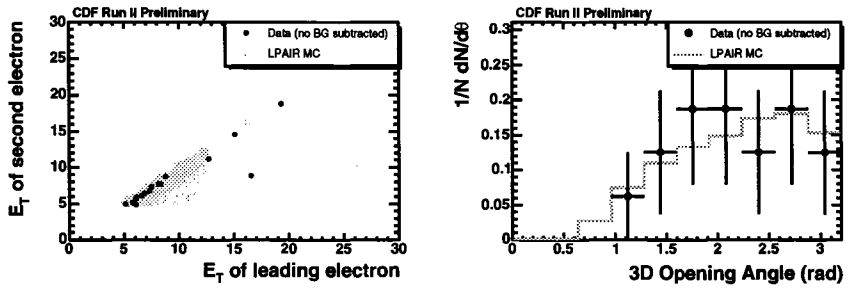

Figure 3.15: E_T of leading electron vs E_T of second electron (left) and 3-D opening angle of ee pairs in signal sample (points) compared to LPAIR MC (line) (right)

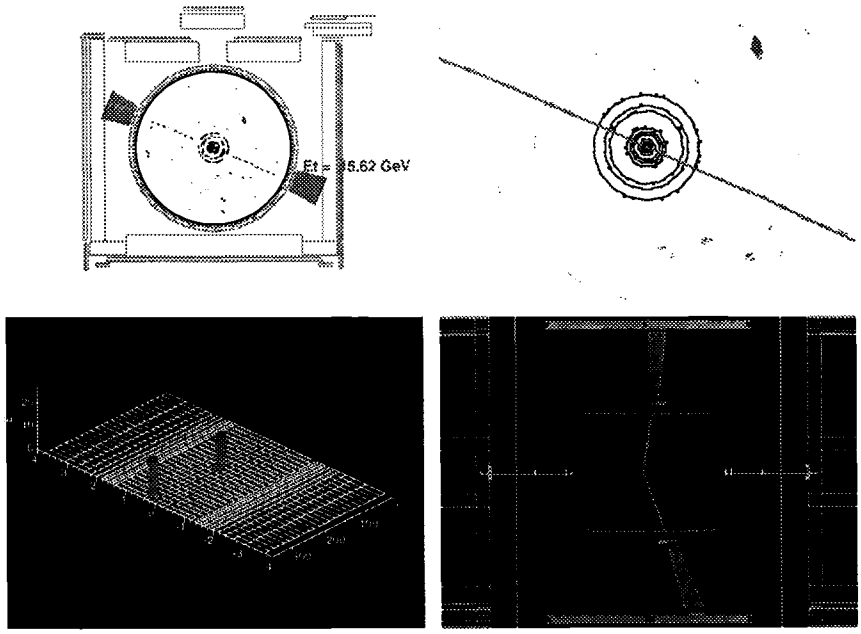

Figure 3.16: Event display of run 195762 event 3788. Note that there is no activity in the calorimeter or COT, other than the two electrons, and that both electrons originate from the beam line.

3.2 Efficiencies

There are four efficiencies to be folded into the cross section calculation:

- ε_{ee}, the efficiency for identifying the two electrons
- ε_{exc}, the efficiency of the exclusivity cuts
- ε_{fsr}, the efficiency for events which undergo some final state radiation
- ε_{cos}, the efficiency of the cosmic cut

Each of these efficiencies will be discussed in the following sections.

3.2.1 Electron Efficiency

The electron efficiency can be broken into four parts; reconstruction efficiency, $\varepsilon_{ee,rec}$, trigger efficiency, $\varepsilon_{e,trig}$, ID efficiency, $\varepsilon_{e,id}$, and tracking efficiency $\varepsilon_{e,trk}$. The reconstruction and trigger efficiencies are both functions of E_T . The expected signal (from LPAIR Monte Carlo) is a steeply falling function of E_T , so the LPAIR E_T distribution must be taken into account for these efficiencies.

The reconstruction efficiency is denoted with subscript "ee", rather than just "e", to reflect the fact that this efficiency must be calculated per event, rather than per electron, because of the ϕ correlation between the two electrons. This notation will be carried throughout the thesis, subscript "ee" meaning per event and subscript "e" meaning per electron. The four parts can be combined to calculate the total electron efficiency:

$$\varepsilon_{ee} = \varepsilon_{ee,rec} \cdot \varepsilon^2_{e,trig} \cdot \varepsilon^2_{e,id} \cdot \varepsilon^2_{e,trk} \tag{3.1}$$

Electron Reconstruction Efficiency, $\varepsilon_{ee,rec}$

The electron reconstruction efficiency, $\varepsilon_{e,rec}$, accounts for electrons that do not get identified as electromagnetic clusters in the offline data - they have fallen into inactive parts of the detector, like the cracks between the ϕ wedges and the crack at η =0 of the calorimeter. Since the two electrons in the event are highly correlated (back-to-back in ϕ and balanced in E_T), the probability of

finding both electrons is not equal to the square of the probability of finding one electron (if one falls into a ϕ crack, the other is more likely to fall into a ϕ crack). Therefore, $\varepsilon_{e,rec}$ is calculated using the LPAIR MC on a per event basis (not per electron). Events generated with LPAIR are put through detector simulation, cdfSim version 5.3.3, and ntuplized with Stntuple dev_242.

Reconstruction efficiency is as defined:

$$\varepsilon_{ee,rec} \equiv \frac{N_{gen+rec}}{N_{gen}} \tag{3.2}$$

The denominator, N_{gen}, is the number of events generated with both electrons having $|\eta| < 2.0$. The numerator, $N_{gen+rec}$, is the number of events from the denominator that have both reconstructed electrons within $\Delta R < 0.4$[4] of the generated electron. A reconstructed electron is any TStnElectron, where a TStnElectron is the loosest definition of an electron available in the CDF off-line code. Using this prescription, the reconstruction efficiency is 0.69±0.02, where the uncertainty is the systematic evaluated by changing the energy scale (E_T cut) by 1%. The choice of 1% is based on the measured accuracy of the calorimeter energy scale in CDFSim. Figures 3.17 and 3.18 show $\varepsilon_{ee,rec}$ as a function of E_T , η , and ϕ .

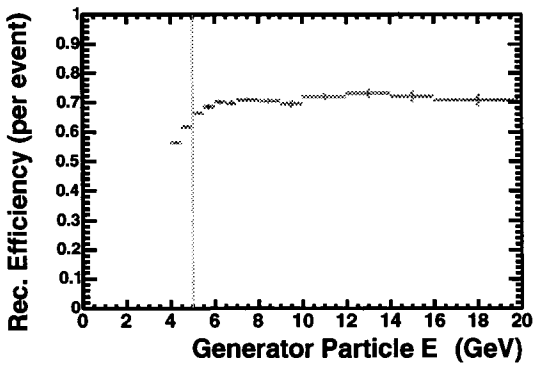

Figure 3.17: Electron reconstruction efficiency, $\varepsilon_{ee,rec}$, as a function of generator electron E_T . The grey line shows the 5 GeV cut.

[4] $\Delta R \equiv \sqrt{\Delta\eta^2 + \Delta\phi^2}$

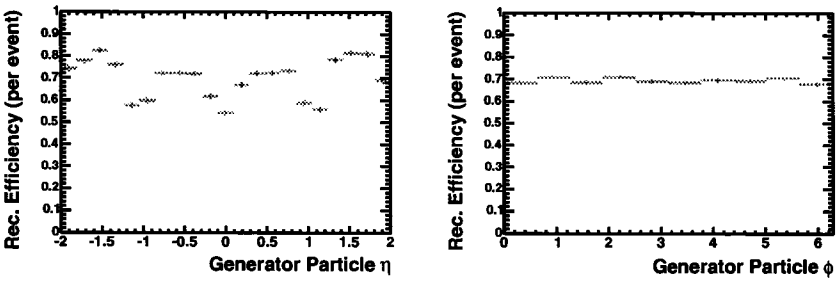

Figure 3.18: Electron reconstruction efficiency, $\varepsilon_{ee,rec}$, as a function of generator electron η and ϕ

Electron ID Efficiency, $\varepsilon_{e,id}$

Central

The simplest way to measure the electron ID efficiency is to obtain a clean (very little background) sample of electrons without using the cuts you wish to examine. The efficiency can then be determined by counting the fraction of electrons from the clean sample that pass the electron ID cuts. To obtain a clean and unbiased sample of electrons, $J/\Psi \rightarrow ee$ events are selected from events that were triggered with only one electron. If the trigger contained two electrons, then there would be a trigger bias in the sample. One of the legs of the J/Ψ is used to tag the J/Ψ , the other is used as a probe to measure the electron efficiency. Efficiency is defined as the number of probe electrons that pass a cut divided by the total number of probe electrons.

$$\varepsilon_{e,id} = \frac{N_{e,probe}^{passIDcuts}}{N_{e,probe}} \tag{3.3}$$

To extract a sample of $J/\Psi \rightarrow ee$ events, we use the "edil0d" dataset stntuplized with CDFSOFT version 5.3.3 and stntuple dev_242 and select events that passed the ELECTRON_CENTRAL_4 trigger. This study can only be done for central electrons because there are no suitable triggers in the plug region. In order to select J/Ψ events we made the following requirements on each event:

- require 2 or 3 TStnElectrons in the event (to reduce combinatoric back-

ground)

- make an array of tight electrons from the TStnElectrons (tight electron cuts are listed in Table 3.6)
- define a probe electron as having:
  - vertex z position within 1 cm of the tight electron
  - opposite charge to the tight electron
  - a seed tower different from that of the tight electron
  - invariant mass between 2.9 GeV/c^2 and 3.3 GeV/c^2

The invariant mass of the tight electrons with the probe electrons (before the mass cut) is shown in Figure 3.19. This shows a clean J/Ψ peak with very little background. Therefore the probe electrons fit the requirement of being clean and unbiased because they were selected without trigger or quality cuts (the TStnElectron requirements are all looser than the ID cuts) and have very little background.

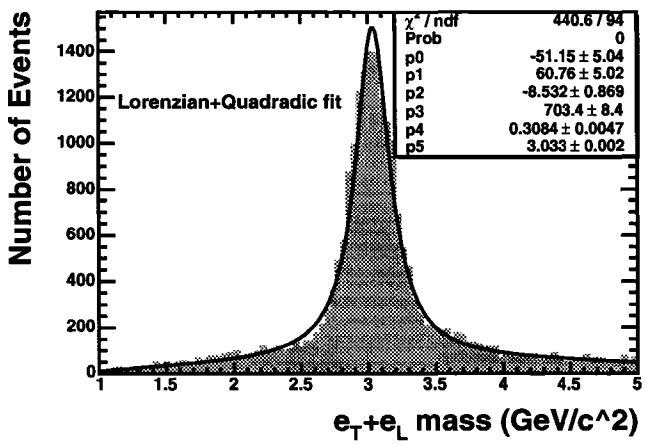

Figure 3.19: Tight + Loose (ie. probe) electron invariant mass which shows a very clean J/Ψ peak.

The efficiency for both Had/Em and CES shape (χ^2) cuts is shown in Figure 3.20 to be 95%±4%. It is independent of E_T , η , and ϕ within the

Variable	Cut
Cluster E_T	> 5.0 GeV
Track energy over momentum	< 2.0
$\|z\|$ position of vertex	< 60 cm
Had/Em	< 0.055+0.00045*E
Iso/E_T	< 0.1
Cluster shoulder energy (Lshr)	< 0.2
Track match in x to CES (DelXQ)	> -3.0 and < 1.5
Track match in z to CES (DelZ)	< 5.0
CES χ^2 (Chi2Strip)	< 10.0
Fiducial in SMX (FidEleSmx)	=1
# of COT superlayers hit (Nssl, Nasl)	> 2

Table 3.6: Tight electron cuts

uncertainty of the measurement. The Had/Em cut is the dominant source of inefficiency, most likely because the probe electrons are not isolated from hadronic activity.

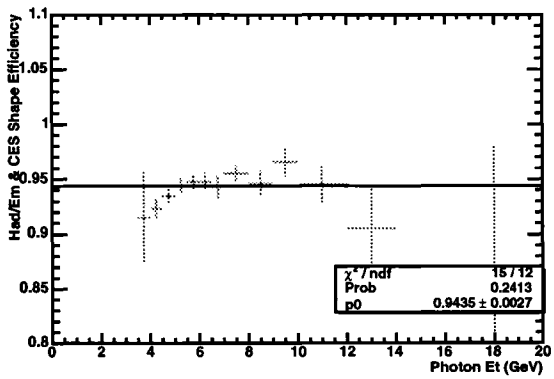

Figure 3.20: Efficiency of the electron ID cuts (Had/Em plus CES shape).

Plug

The above data set used to calculate the central electron ID efficiency can not simply be extended to look at electrons in the plug, because the trigger is based on a central EM cluster, and most $J/\Psi \rightarrow ee$ events produce two electrons that are close together - so they are unlikely to have probe electrons

in the plug region. However, a similar study of plug electrons in the E_T region of interest has been done using Drell-Yan events. The result is a Had/Em efficiency of 99%±1% and a PES shape (χ^2) efficiency of 88%±2%. The total plug electron ID efficiency is 87%±3%.

Overall Electron ID Efficiency

The overall electron ID efficiency can now be calculated based on the expected fraction of electrons in the central and plug regions. LPAIR MC predicts that 63% of reconstructed electrons with $E_T > 5.0$ GeV and $\eta < 2.0$ fall in the central region, and 37% in the plug region. Weighting the central and plug ID efficiencies by 0.63 and 0.37 respectively, the overall electron ID efficiency (per electron) is 0.92±0.04.

Electron Trigger Efficiency, $\varepsilon_{e,trig}$

The trigger efficiency accounts for those electrons that would get reconstructed and pass all off-line ID criteria, but fail the trigger. The trigger efficiency, ε_{trig}, can be defined as

$$\varepsilon_{e,trig} \equiv \frac{N_{trig+id}}{N_{id}} \tag{3.4}$$

The denominator, N_{id}, are electrons selected from minbias[5] data as electrons that pass all the ID cuts. Using minbias data gives a sample with no trigger bias on the electrons. The numerator, $N_{trig+id}$, is found by determining how many of the N_{id} sample would have passed the electron trigger requirements (a match between a trigger and off-line electron is defined as having the same seed tower).

To determine whether or not they would pass the trigger requirements the Level 2 and Level 3 triggers were simulated using the trigger information recorded in the off-line event record. Level 1 has no effect on the trigger efficiency because any electron which passes the L2 trigger will pass the L1 trigger (a L2 EM cluster in the DIFF_DIPHOTON trigger a 'single-tower' cluster like L1).

[5]minbias means data taken with the minimum bias trigger, an east-west coincidence of the CLC detectors

The trigger efficiency as a function of E_T , η , and ϕ is shown in Figures 3.21 and 3.22. The trigger efficiency as a function of E_T must be applied to the expected signal sample because the E_T distribution in exclusive events is slightly steeper than that of the EM clusters in minbias data. $\varepsilon_{e,trig}$ is calculated from Figure 3.23 as the total number of LPAIR events times the efficiency (filled histogram) divided by the number of LPAIR events (empty histogram). The efficiency as a function of E_T is also shown on Figure 3.23. This weighting does not need to be done for the η distribution, since the minbias and expected signal distribution are similar in η . The integrated trigger efficiency is therefore 0.77±0.05, where the systematic uncertainty is evaluated by varying the value of the trigger efficiency (for each bin) by the upper and lower bounds of the efficiency as a function of E_T .

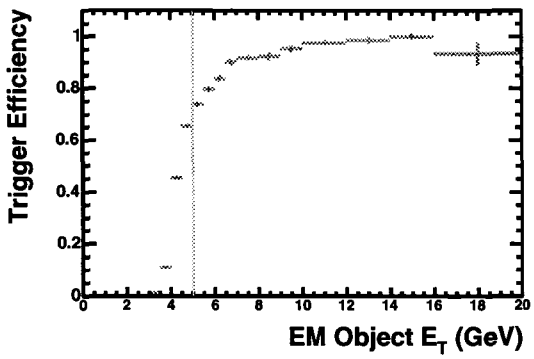

Figure 3.21: Electron trigger efficiency, $\varepsilon_{e,trig}$, as a function of off-line E_T

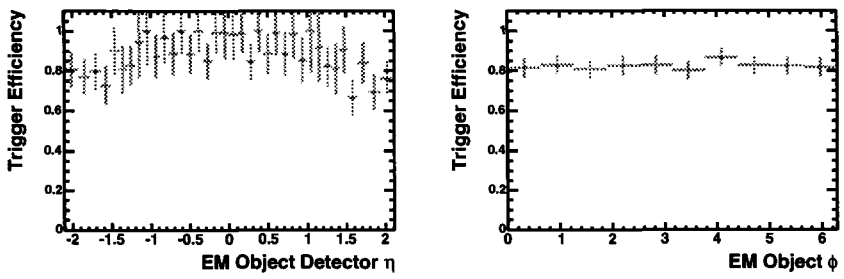

Figure 3.22: Electron trigger efficiency, $\varepsilon_{e,trig}$, as a function of off-line η and ϕ

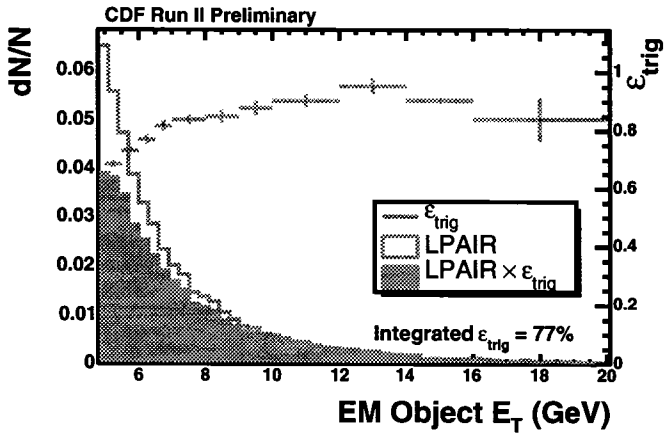

Figure 3.23: The overall electron trigger efficiency, $\varepsilon_{e,trig}$, is calculated as the integral of the closed histogram divided by the integral of the open histogram.

Electron Tracking Efficiency, $\varepsilon_{e,trk}$

The tracking efficiency can be defined as:

$$\varepsilon_{e,trk} = \frac{N_{e,probe}^{pass\ track\ cut}}{N_{e,probe}} \tag{3.5}$$

Where the numerator, $N_{e,probe}^{pass\ track\ cut}$ is the number of probe electrons with NTracks = 1 and that track having p_T >1 GeV/c, and the denominator, $N_{e,probe}$, is the number of probe electrons. The probe electrons in this case are taken from $Z \rightarrow ee$ events where the Z is identified using electrons constructed with their calorimeter properties. If an electron from a pair in the mass window 80 GeV/c^2 to 100 GeV/c^2 has a track, then the other electron is used as the probe. Figure 3.24 shows that the tracking efficiency is ~99% in the central region, and drops to ~20% at η =2. The efficiency as a function of η is then integrated with the reconstructed electron η distribution from LPAIR in Figure 3.25, which shows the overall tracking efficiency is 87% (per electron).

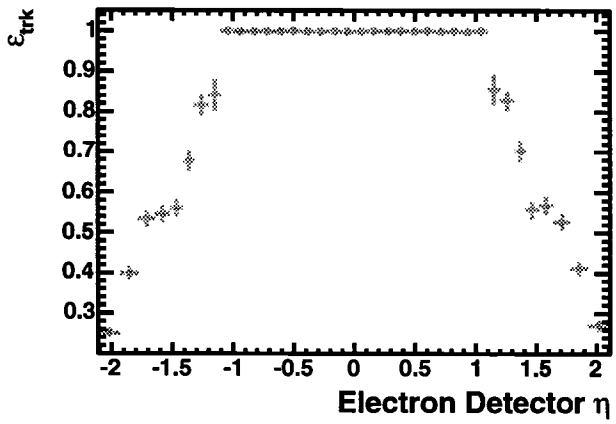

Figure 3.24: Tracking efficiency.

$\varepsilon_{ee,rec}$	0.69±0.02
$\varepsilon_{e,trig}$	0.77±0.05
$\varepsilon_{e,id}$	0.92 ± 0.04
$\varepsilon_{e,track}$	0.87 ± 0.05
ε_{ee}	0.26 ± 0.03

Table 3.7: Summary of electron efficiencies

Overall Electron Efficiency

From the summary of the electron efficiencies shown in Table 3.7, the overall electron pair efficiency is calculated to be:

$$\varepsilon_{ee} = \varepsilon_{ee,rec} \cdot \varepsilon^2_{e,trig} \cdot \varepsilon^2_{e,id} \cdot \varepsilon^2_{e,trk} = 0.26 \pm 0.03 \tag{3.6}$$

3.2.2 Final State Radiation Efficiency, ε_{fsr}

If one of the final state electrons in a $p\bar{p} \rightarrow p + ee + \bar{p}$ interaction emits enough bremsstrahlung radiation, it is possible for there to be energy deposited outside the electron towers. This would prevent the event from being counted as a signal event because all the energy outside the electron towers is vetoed in the exclusive cuts. This is not accounted for in ε_{exc} because that is based entirely on the state of the detector, not the details of the signal. To estimate ε_{fsr} we

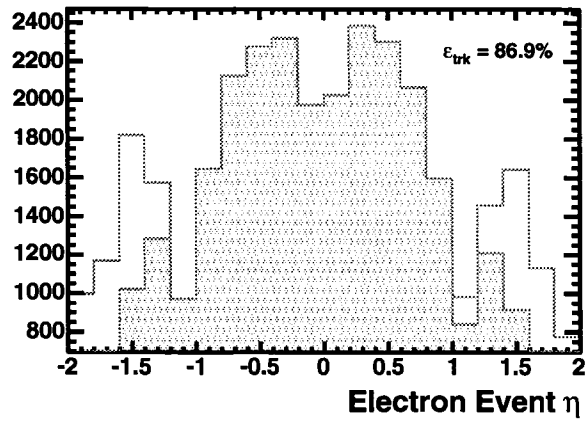

Figure 3.25: LPAIR η distribution (empty histogram) and the LPAIR η distribution weighted by the tracking efficiency in that η bin (filled histogram).

run a sample of LPAIR Monte Carlo events through the exclusive cuts. ε_{fsr} can then be defined as:

$$\varepsilon_{fsr} = \frac{N_{LPAIR}^{pass\ exc\ cuts}}{N_{LPAIR}} \tag{3.7}$$

Where the denominator, N_{LPAIR} is the number of LPAIR events with both electrons in $|\eta| < 2$ and E_T >5 GeV. The numerator is the number of denominator events that pass the exclusive cuts described in the event selection, Section 3.1.4. This calculation gives ε_{fsr}=0.79±0.05.

3.2.3 Cosmic Efficiency, ε_{cos}

The efficiency of the cosmic ray cut is determined by selecting a sample of non-cosmic electron pairs with the following cuts:

- Track D_o < 2 cm
- 3-D opening angle < 2.6 rad
- Seed Tower < tower 18 (EM Timing is not available for towers 18 and greater)

The cosmic efficiency, ε_{cos}, is then defined as:

$$\varepsilon_{cos} \equiv \frac{N_{NonCosmic}^{pass\ cosmic\ cut}}{N_{NonCosmic}} \tag{3.8}$$

Where, $N_{NonCosmic}$ is the number of events passing the non-cosmic cuts above, and $N_{NonCosmic}^{pass\ cosmic\ cut}$ is the number of $N_{NonCosmic}$ events that pass the cosmic cuts outlined in Section 3.1.3.

A plot of the EM time for non-cosmic events is shown in Figure 3.26. 93% of anticosmic events have both electrons within the cut window, therefore, ε_{cos} = 0.93±0.03. A systematic was evaluated by shifting the cosmic cut by the resolution of the EM timing system. The events in the -99 bin are events that did not have EM timing information available - this is the dominant source of the inefficiency. The reason electrons may not have EM timing information is that the tower energy is below the threshold for EM timing information (~4 GeV).

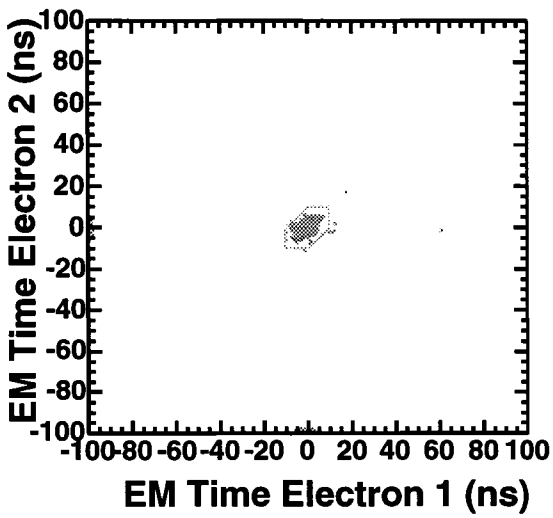

Figure 3.26: EM time of electron 1 vs. electron 2 for non-cosmic events are plotted. Bin -99 corresponds to events with no EM timing information available.

3.2.4 Exclusive Efficiency

Since an inelastic $p\bar{p}$ interaction on top of an exclusive interaction in a beam crossing will make the exclusive interaction unobservable, ε_{exc} is highly dependent on the bunch luminosity[6], $\mathscr{L}_{bunch}$. The details of the ε_{exc} calculation is divided into three subsections; determining $\mathscr{L}_{bunch}$, measuring ε_{exc} as a function of $\mathscr{L}_{bunch}$, and integrating ε_{exc} into the $\mathscr{L}_{bunch}$ distribution.

Determining $\mathscr{L}_{bunch}$

At CDF, $\mathscr{L}_{inst}$ is defined as the sum of the instantaneous luminosities of all 36 bunches circulating in the Tevatron. To determine $\mathscr{L}_{bunch}$ of an event, a weight, W_b, for each bunch in a run is calculated. The weight is the luminosity of the bunch relative to the mean luminosity of the 36 bunches ($W_b = \frac{\mathscr{L}_{bunch}}{\langle \mathscr{L}_{bunch} \rangle}$). The bunch weight can then be used to determine the $\mathscr{L}_{bunch}$ from the $\mathscr{L}_{inst}$; $\mathscr{L}_{bunch} = W_b \cdot \mathscr{L}_{inst}/36$,

Using this presciption requires the assumption that the W_b remains constant for the duration of the run. By looking at W_b at the begining and end of a very long run, the assumption that it remains constant can be tested. The bunch weight stays constant to within 5% in run 206537[7]. This means that the assumption that W_b is constant over the run is adequate.

Measuring ε_{exc} as a Function of $\mathscr{L}_{bunch}$

The exclusive efficiency, ε_{exc}, is defined as:

$$\varepsilon_{exc} \equiv \frac{N_{exc}^{observed}}{N_{exc}^{truth}} = 1 - \frac{N_{exc}^{spoiled}}{N_{exc}^{truth}} \tag{3.9}$$

where $N_{exc}^{observed}$ is the number of exclusive interactions observed in the data sample, N_{exc}^{truth} is the true number of exclusive interactions in the data sample, and $N_{exc}^{spoiled} = N_{exc}^{truth} - N_{exc}^{observed}$. An exclusive interaction can be spoiled by another inelastic $p\bar{p}$ interaction in the beam crossing, a particle entering the detector that was not part of an interaction (beam halo or cosmic ray),

[6]The bunch luminosity is the instantaneous luminosity of the bunch crossing

[7]Initial luminosity = 125×10^{30} $cm^{-2}s^{-1}$, final luminosity = 18×10^{30} $cm^{-2}s^{-1}$, duration = 25 hours

or noise in any of the detectors used to define the exclusive interaction (the calorimeters and BSC).

In order to calculate the fraction $\frac{N_{exc}^{spoiled}}{N_{exc}^{truth}}$ we note that the probability of an exclusive interaction occuring in a beam crossing is independent of any of the factors that can spoil it (cosmic ray, beam halo, noise, or multiple inelastic interaction occuring in the same beam crossing). Therefore, the definition that the final state of an exclusive interaction contains only the outgoing hadrons and the central system (ie. two electrons), the following is evident:

$$\frac{N_{exc}^{spoiled}}{N_{exc}^{truth}} = \frac{N_{BC}^{spoiled}}{N_{BC}} \tag{3.10}$$

where $N_{BC}^{spoiled}$ is the number of beam crossings with any effect that would spoil the ability to observe the exclusivity of an interaction, and N_{BC} is the total number of beam crossings. In other words, the exclusive efficiency is the probability that an exclusive interaction could be observed in the detector if an exclusive interaction occured. From equations 3.9 and 3.10, and the fact that zerobias data is an unbiased sample of beam crossings:

$$\varepsilon_{exc} = 1 - \frac{N_{BC}^{spoiled}}{N_{BC}^{total}} = 1 - \frac{N_{ZB}^{fail}}{N_{ZB}^{total}} = \frac{N_{ZB}^{pass}}{N_{ZB}^{total}} \tag{3.11}$$

where $N_{ZB}^{fail(pass)}$ is the number of zerobias events that fail (pass) all of the exclusive cuts, and N_{ZB}^{total} is the total number of zerobias events in the data sample. Of course, $N_{ZB}^{pass} = N_{ZB}^{total} - N_{ZB}^{fail}$, therefore

$$\varepsilon_{exc} = \frac{N_{ZB}^{pass}}{N_{ZB}^{total}} \tag{3.12}$$

Therefore, ε_{exc} can be determined from zerobias data. It is important to do this over the same run range as the signal data, since the beam effects and electronic noise are run dependent. Figure 3.27 is a plot of ε_{exc} as a function of bunch luminosity for the same good run list used for the event selection. Figure 3.28 shows the n-1 exclusive efficiency for each detector region.

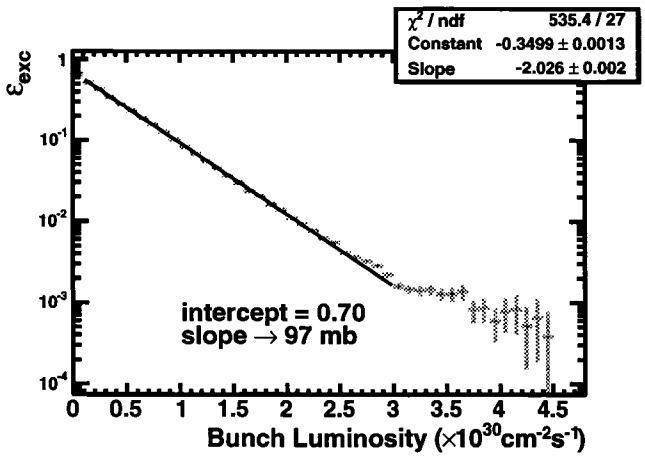

Figure 3.27: Exclusive efficiency as a function of bunch luminosity. The fit curve is only a guide, it is not used to calculate the effective luminosity. The slope and intercept calculation shown indicate the level of inefficiency; if the cuts were perfect the intercept would be 1.0 and the cross section would be 60mb. The higher σ indicates that the cuts are conservative.

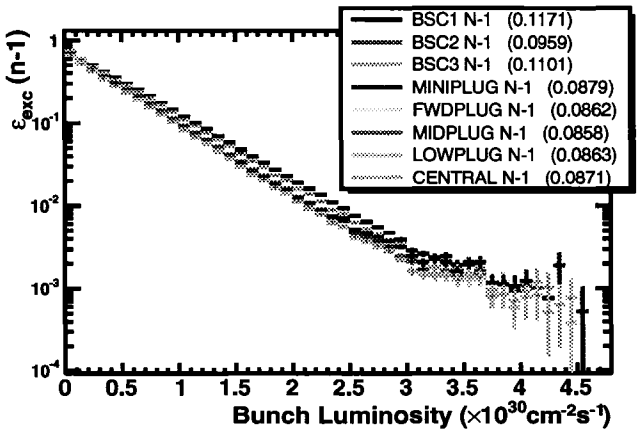

Figure 3.28: The n-1 efficiency as a function of instantaneous luminosity for each of the exclusive cuts.

Integrating ε_{exc} into $\mathscr{L}_{bunch}$ Distribution

The total number of crossings in which an exclusive interaction can be observed, N_O, and the total number of crossings, N_T, can be written as:

$$N_O \propto \int \varepsilon_{exc}(\mathscr{L}) \cdot \mathscr{L}\ dt \tag{3.13}$$

$$N_T \propto \int \mathscr{L}\ dt \tag{3.14}$$

Note that $N_O(\mathscr{L})/N_T(\mathscr{L}) = N_{ZB}^{pass}(\mathscr{L})/N_{ZB}^{total}(\mathscr{L}) = \varepsilon_{exc}(\mathscr{L})$, where $\mathscr{L}$ refers to the bunch luminosity. N_O and N_T can also be written as an integral over the bunch luminosity:

$$N_O \propto \int \varepsilon_{exc}(\mathscr{L}) \cdot N_T(\mathscr{L}) \cdot \mathscr{L}\ d\mathscr{L} \tag{3.15}$$

$$N_T \propto \int N_T(\mathscr{L}) \cdot \mathscr{L}\ d\mathscr{L} \tag{3.16}$$

Taking the ratio of N_O to N_T, with equations 3.14 and 3.16, one gets:

$$\frac{N_O}{N_T} = \frac{\int \varepsilon_{exc}(\mathscr{L}) \cdot \mathscr{L}\ dt}{\int \mathscr{L}\ dt} = \frac{\int \varepsilon_{exc}(\mathscr{L}) \cdot N_T(\mathscr{L}) \cdot \mathscr{L}\ d\mathscr{L}}{\int N_T(\mathscr{L}) \cdot \mathscr{L}\ d\mathscr{L}} \tag{3.17}$$

Therefore:

$$\int \varepsilon_{exc}(\mathscr{L})\mathscr{L} dt = \frac{\int \varepsilon_{exc}(\mathscr{L}) \cdot N_T(\mathscr{L}) \cdot \mathscr{L}\ d\mathscr{L}}{\int N_T(\mathscr{L}) \cdot \mathscr{L}\ d\mathscr{L}} \int \mathscr{L} dt \tag{3.18}$$

And so the exclusive efficiency integrated over the bunch luminosity of the data sample can be defined as:

$$\varepsilon_{exc} = \frac{\int \varepsilon_{exc}(\mathscr{L}) \cdot N_T(\mathscr{L}) \cdot \mathscr{L}\ d\mathscr{L}}{\int N_T(\mathscr{L}) \cdot \mathscr{L}\ d\mathscr{L}} \tag{3.19}$$

The overall exclusive efficiency, ε_{exc}, can now be calculated with Equation 3.19 and Figure 3.29. The open histogram is the $\mathscr{L}_{bunch}$ distribution for all zerobias data in the good run range weighted by $\mathscr{L}_{bunch}$, the points are ε_{exc} (note that the scale for ε_{exc} is on the right), and the filled histogram is the weighted $\mathscr{L}_{bunch} \cdot \varepsilon_{exc}$. The overall exclusive efficiency is therefore equal to the integral of the filled histogram ($\int \varepsilon_{exc} \cdot N\ d\mathscr{L}$), divided by the integral of the open histogram ($\int \cdot N\ d\mathscr{L}$). The result is $\varepsilon_{exc} = 0.0856$. The systematic uncertainties in this number either cancel out (because a change in the exclusive cut will change the number of events observed) or they are accounted for in the uncertainly in the luminosity already applied to the integrated luminosity.

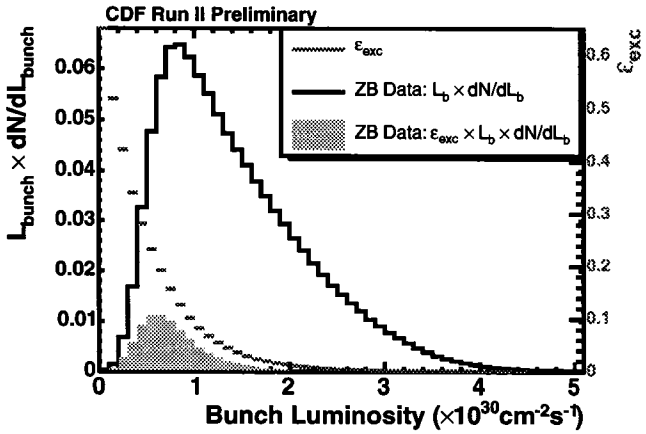

Figure 3.29: $\mathscr{L}_{bunch}$ distribution for all zerobias data (open histogram with scale on left), ε_{exc} (points with scale on right), and weighted $\mathscr{L}_{bunch} \times \varepsilon_{exc}$ (filled histogram with scale on left) for calculation of ε_{exc}=0.0856

3.3 Backgrounds

There are four backgrounds to consider:

'Jet' fake background due to something other than an electron appearing to be an electron by passing the electron cuts.

Cosmic background due to cosmic rays occuring in time with the beam crossing and passing all electron and exclusive cuts.

Exclusivity background due to inclusive processes (ie. Drell-Yan) that appear exclusive due to particles not being observed in the calorimeters (ie. falling into cracks in the detector or being too soft to reach any detectors)

Dissociation background due to inelastic $\gamma\gamma \rightarrow e^+e^-$ events where the dissociation products are too far forward to be detected by the BSCs (see Figure 1.6b and 1.6c).

3.3.1 'Jet' Fake Background

The jet fake rate (F_{jet}) is the probability that a hadron fakes an electron by passing the electron cuts. The jet fake rate for this analysis is defined as the probability that a single-track jet[8] passes the electron cuts.

$$F_{jet} \equiv \frac{N_{jets}^{pass\ electron\ cuts}(|\eta| < 2,\ NTracks = 1,\ TrackPt > 1.0)}{N_{jets}(|\eta| < 2,\ NTracks = 1,\ TrackPt > 1.0)} \tag{3.20}$$

Where the denominator, $N_{jets}(|\eta| < 2,\ NTracks = 1,\ TrackPt > 1.0)$ is the number of jets in GAP_GAP_ST5 trigger data (the same good run list as the signal sample) with $|\eta| < 2$, $NTracks = 1$, $TrackPt > 1.0$. The numerator, $N_{jets}^{pass\ electron\ cuts}(|\eta| < 2,\ NTracks = 1,\ TrackPt > 1.0)$ is the number of denominator jets that pass the electron cuts listed in Table 4.1 plus the single-track with p_T >1.0 GeV/c requirement. Figure 3.30 shows F_{jet} is <2%[9], and does not have significant dependence on E_T .

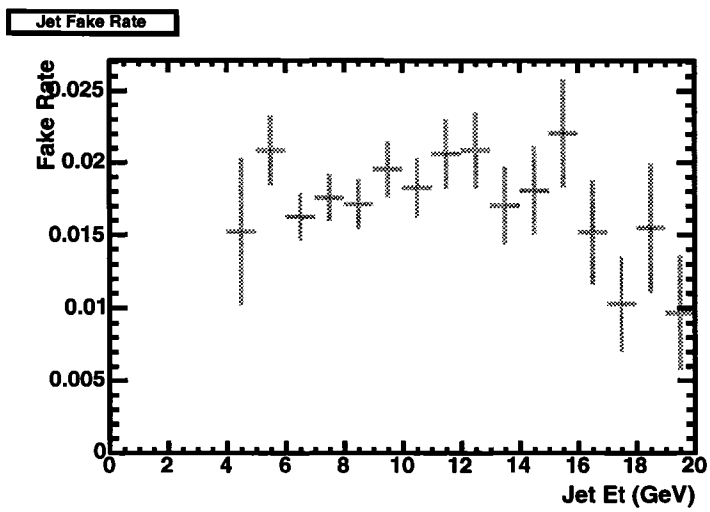

Figure 3.30: Jet fake rate (F_{jet}) is <2%

Naively, the jet fake background could be estimated by estimating the number of events with two exclusive jets expected in the data sample, $N_{jj}^{pass\ all\ exc\ cuts}$,

[8]'single-track' is specified because a multi-track jet does not fake the signal which requires only 1 track

[9]the numerator 'jets' could actually be electrons

and then weighting each jet by F_{jet}. However, F_{jet} is a calculation of the ratio of *inclusive* jets faking electrons, not *exclusive* jets faking electrons. This means that we can not apply the exclusivity requirement to the jet if we want to weight it by F_{jet}. To avoid this difficulty, F_{jet} will be applied to all jets in the GAP_GAP_ST5 trigger data that pass the exclusivity cuts in the $|\eta| > 2$ region. This means that we will get an upper limit on the jet fake background, since $N_{jj}^{pass\ all\ exc\ cuts} < N_{jj}^{pass\ |\eta|>2\ exc\ cuts}$, while avoiding the application of the exclusivity requirement to the jets which are all in $|\eta| < 2$.

There are no events in the GAP_GAP_ST5 trigger data with two single-track jets passing the exclusive cuts for $|\eta| > 2$. Therefore, to 95% CL, there are less than 3.1 events with two single-track jets which pass the exclusive cuts. However, there is a factor 100 prescale on the GAP_GAP_ST5 trigger, therefore $N_{jj}^{pass\ all\ exc\ cuts} < 310$. Applying F_{jet} to each jet, gives an upper limit of $310 \cdot (0.02)^2 = 0.12$ background events. This estimate is an upper limit, so the jet fake background can be conservatively written as $0.0^{+0.1}_{-0.0}$ events.

3.3.2 Cosmic Background

The background from cosmic rays falling within the cosmic cuts can be evaluated by measuring the density of events outside the cosmic cuts and then extrapolating that density into the cut region. Figure 3.31 is a plot of the EM time of all electron candidates (with no track cut) in the DIFF_DIPHOTON trigger sample (black) and the non-cosmic events (red). There are 514 events in the 9700 ns^2 area outside the signal region, so the density of background events is 0.0530 events/ns^2. The signal region is 300 ns^2, so we can expect 15.9 of the 67502 events in signal region to be cosmic. Therefore the probability of a two electron event that passes the cosmic cuts actually being a cosmic is 2.3×10^{-4}. This corresponds to a negligible number of background events in the 16 event signal sample.

3.3.3 Exclusivity Background

The exclusivity background accounts for non-exclusive events where some particle(s) passed through the cracks in the calorimetry coverage or below the

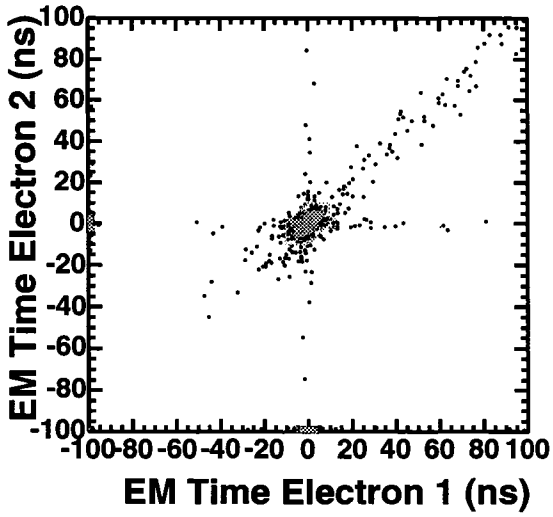

Figure 3.31: The cosmic background fraction is estimated to be 2.3×10^{-4}. There are more cosmic ray events with time greater than zero because the gate of the timing system is not symmetric around the bunch crossing time so clusters with high negative values are not recorded.

noise thresholds, causing them to appear exclusive. Z boson events provide an ideal sample to test the ability of the calorimeters to observe exclusive events because Z can not be produced exclusively and it decays to two electrons. Events from the two candidate sample (with tracks) are compared to Z events as a function of the number of associated towers[10] in Figure 3.32.

Figure 3.32 shows a very clear peak above a very small background. In order to estimate the amount of background in the zero bin (the signal region), the number of data events in the 5 to 20 bins are averaged over all 15 bins. 3 events in 15 bins, comes out to 0.2 events per bin. Because there is no evidence the exclusive background actually results in any background events, this estimate is taken as an upper limit, making the exclusivity background $0.0^{+0.2}_{-0.0}$.

A potentially significant difference between the signal sample of this anal-

[10]An associated tower is a tower that is not an electron tower but is above the exclusive cut threshold.

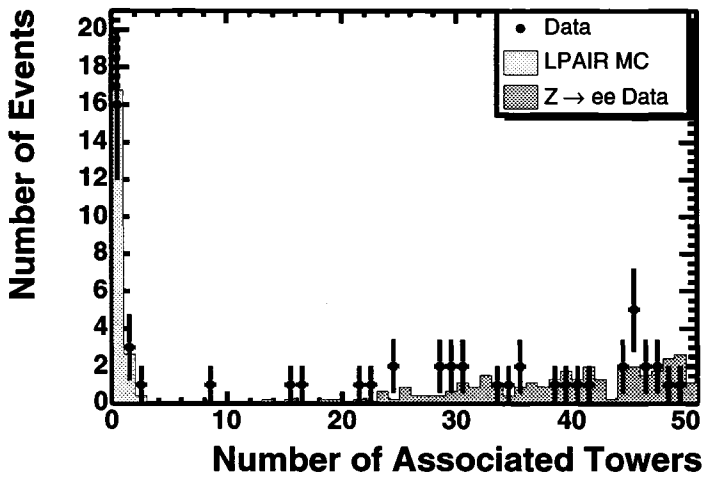

Figure 3.32: Number of associated towers for LPAIR MC, Z→ee data, and the electron sample (with no BSC cuts applied). LPAIR MC is normalized to events below 5 towers, Z→ee data is normalized to the events above 5 towers.

ysis and the Z→ee data is the E_T of the electrons being considered. Z→ee electrons have much higher E_T than those in the signal sample. To investigate this potential complication, a Drell-Yan MC was used in place of the Z→ee data in Figure 3.33. It shows the same result, a very small background on top a very clear peak. This is a cross check, not an additional background, so it does not add anything but confidence to the previous background estimate. The important observation for both the Drell-Yan MC and the Z→ee data is that there is no enhancement near the signal region - this means that the background can be extrapolated from the sideband of the data distribution.

3.3.4 Dissociation Background

The dissociation background accounts for events that are mediated by two-photon exchange, but instead of being truly exclusive, one or both of the protons is excited into a low mass state and then dissociates. It is possible for these dissociations to be contained in $|\eta| > 7.4$, and hence they would not be observable in the CDF detector. The inelastic running mode of LPAIR MC

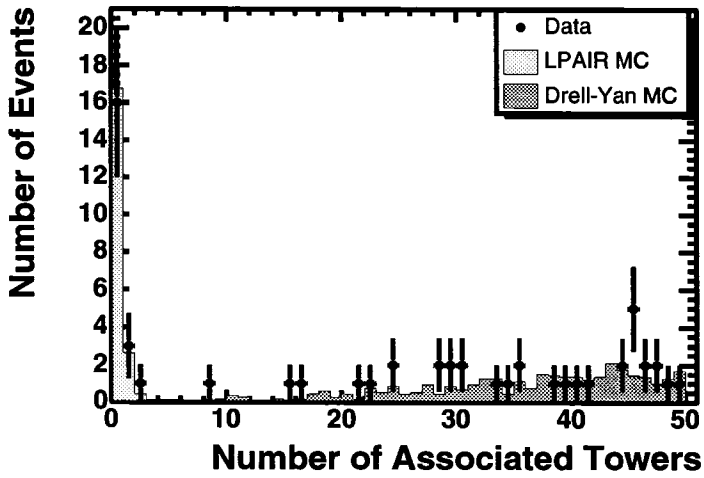

Figure 3.33: Number of associated towers for LPAIR MC, Drell-Yan MC, and the electron sample. LPAIR MC is normalized to events below 5 towers, Drell-Yan MC is normalized to the events above 5 towers.

(see Figure 1.6b and 1.6c) is used to estimate this background. Unfortunately, LPAIR MC only provides the kinematics of the dissociating proton, it does not actually dissociate the system. To dissociate the system, a function called 'fragment_cluster' from Minimum Bias Rockefeller (MBR) MC is used. This function fragments a cluster into hadrons, and then boosts the system back into the laboratory frame. Figure 3.34 shows the fraction of proton dissociations whose fragments would all remain in the region greater than the η cut. It shows that 7% of dissociating protons from LPAIR events with electrons in $E_T > 5.0$ GeV and $\eta < 2.0$ have no particles with $|eta| < 7.4$.

To get the probability of a blind dissociation[11], P_{BD}, the efficiency of the BSC3 detectors, ε_{BSC3} must be taken into account. Each BSC3 detector is divided into two separate (non-overlapping) scintillator counters; each counter is read out by a PMT. In order to determine ε_{BSC3}, the ADC distribution of each counter was examined for events that had a hit in the other counter (using minbias data). Figure 3.35 shows the efficiency for each of the 4 PMTs

[11]Blind dissociation meaning a dissociation that was not observed in the BSC.

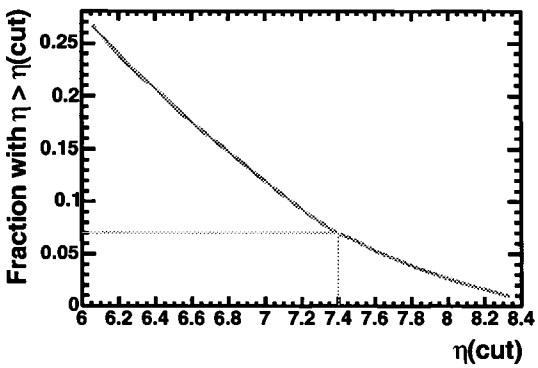

Figure 3.34: The fraction of proton dissociations whose fragments would all remain in region greater than the η cut.

in BSC3 (2 PMTs on east side, 2 PMTs on west side) is 0.9±0.1. Since the denominator is does not always correspond to a particle in the channel, this efficiency is really a lower limit. Therefore, $P_{BD} = 0.07/0.9 = 0.08 \pm 0.01$, where the systematic uncertainty is dominated by the uncertainty in the BSC3 efficiency.

To determine how many background events this corresponds to, P_{BD} must be factored into the cross section for the proton dissociation events. LPAIR MC predicts that $\sigma_{inel-el} = 1.54$ pb, $\sigma_{inel-inel} = 1.48$ pb, and $\sigma_{el-el} = 1.71$ pb. Taking these and P_{BD} into account, the cross section for a blind dissociation event is $\sigma_{BD} = 0.25$ pb[12]. All events in the candidate sample correspond to $\sigma_{Cand} = 1.71 + 0.25 = 1.96$ pb, so the fraction of events in the candidate sample is F_{BD}=0.13±0.02, where the uncertainty comes from the systematic uncertainty on P_{BD}, since the uncertainties on the LPAIR predicted cross sections are negligible. This corresponds to 2.1±0.3 events in the 16 events of the signal sample.

There is a process called the Deck effect which is related to the dissociation background but considers the proton's $\pi^{\pm}$ field as the source of the fusing photons. This process is expected to be at least an order of magnitude smaller than the dissociation process considered [34]

[12] $\sigma_{BD} = 2P_{BD}\sigma_{inel-el} + P_{BD}^2\sigma_{inel-inel} = 0.25$ pb

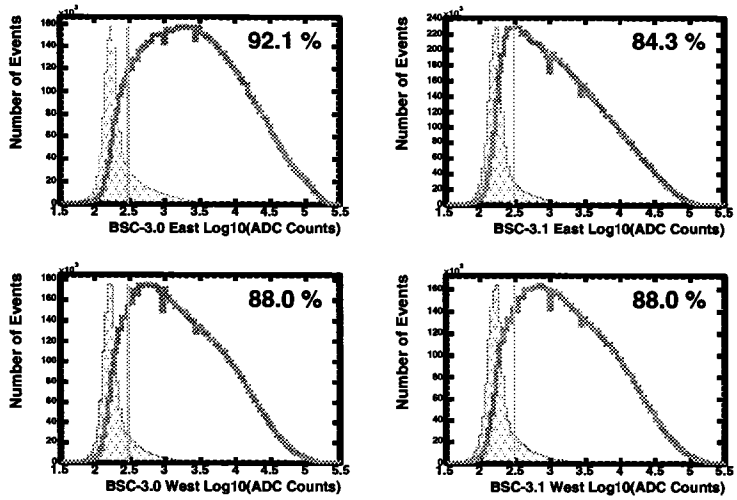

Figure 3.35: Plots show the number of events with a hit (ADC counts>400) in a PMT, given that there was (empty histogram) or was not (filled histogram) a hit in the adjacent PMT. The efficiency is the fraction of events in the empty histogram above 400 counts divided by the number of events in the empty histogram.

3.3.5 Background Summary

A summary of the backgrounds is listed in Table 3.8.

Background	Value	Uncertainty
jet fake	0.0	$^{+0.1}_{-0.0}$
cosmic	negligible	negligible
exclusive	0.0	$^{+0.2}_{-0.0}$
dissociation	2.1	0.3
total	2.1	$^{+0.6}_{-0.3}$

Table 3.8: Summary of background numbers put into the cross section calculation.

Quantity	Value	Uncertainty
N_{sig}	16	$^{+5.1}_{-3.2}$ (stat)
N_{bkgd}	2.1	$^{+0.6}_{-0.3}$ (sys)
$\mathscr{L}$	532	32 (sys)
ε_{exc}	0.0856	n/a
ε_{cos}	0.93	0.03 (sys)
ε_{fsr}	0.79	0.05 (sys)
ε_{ee}	0.26	0.03 (sys)

Table 3.9: Summary of numbers put into the cross section calculation.

3.4 Cross Section

The cross section for elastic-elastic production of electron pairs with E_T (e) > 5.0 GeV, $|\eta|$ < 2.0 at the Tevatron, $\sqrt{s}$ = 1960 GeV, is predicted by LPAIR MC to be σ_{peep} = 1.711±0.008 pb.

A signal of 16 exclusive electron pair production events ($|\eta|(e)$ < 2.0 and $E_T(e)$ >5 GeV) have been observed with a background estimate of 2.1 $^{+0.6}_{-0.3}$ events. The events are consistent in both their cross section and kinematic distributions with $pp \rightarrow p + e^+e^- + p$ through two photon exchange. Using Equation 3.21 and the numbers in Table 3.9 the cross section for exclusive electron pair production is measured to be $\sigma_{exc,ee}^{E_T>5\ GeV,|\eta|<2} = 1.6^{+0.5}_{-0.3}$(stat) ± 0.3(sys) pb. This agrees with the theoretical cross section of 1.711±0.008 pb from LPAIR MC.

$$\sigma_{exc,ee}^{E_t>5\ GeV,|\eta|<2} = \frac{N_{sig} - N_{bkgd}}{\varepsilon_{cos} \cdot \varepsilon_{fsr} \cdot \varepsilon_{ee} \cdot \varepsilon_{exc} \cdot \int \mathscr{L}} \tag{3.21}$$

There is a 3.0×10^{-8} Poisson probability that 2.7 events (the upper limit of the background estimate) fluctuates to 16 or more events. The integral of a one-sided normalized Gaussian distribution greater than 5.5σ is 3.0×10^{-8}. The significance of this result is therefore quoted as 5.5σ. This is the first time any exclusive two-photon process has been observed in hadron-hadron collisions.

Chapter 4

Evidence of Exclusive $\gamma\gamma$ Production

This chapter details the analysis showing evidence for the QCD mediated exclusive $\gamma\gamma$ process. Since the e^+e^- analysis is nearly identical from a detector point of view, this chapter relies heavily on the previous chapter. The format of this chapter is similar to the previous, with sections on event selection, efficiency, background, finally a calculation of the cross section of exclusive $\gamma\gamma$.

4.1 Event Selection

4.1.1 Trigger and Good Run Lists

The DIFF_DIPHOTON trigger and good run lists used for this analysis are the same as in the previous chapter, see 3.1.1.

4.1.2 Photon ID Cuts

The exclusive e^+e^- analysis uses both the central and plug regions. Because the tracking efficiency drops in the plug region, e^+e^- events with no tracks would become a background to the $\gamma\gamma$ events. In order to minimize background this analysis will only include the central region, where the tracking efficiency is 99%. Other than the η range and the tracking requirements, the ID cuts in this analysis are identical to the ID cuts used in the e^+e^- analysis. For clarity, the central region of Table 4.1 is copied here from the previous chapter.

Cut	Threshold
Energy (GeV)	$E_T > 5.0$
Shower Shape	CES χ^2 <20
Had/Em Ratio	< 0.055 + 0.00045*E
CES Fiducial	$\|x\|$ <21.0, 9.0<z<230.0

Table 4.1: Details of central photon ID cuts (energy units are GeV).

Cut	Threshold
$\Delta\cot(\theta)$	<0.1
XY Separation	<0.9 cm

Table 4.2: Conversion Cuts.

4.1.3 Cosmic Ray Cut

The cosmic rays cuts are the same as the e^+e^- analysis, see Section 3.1.3

4.1.4 Exclusivity Cuts

The choice of cuts to define empty regions of the detector is described in Section 3.1.4.

4.1.5 Track Cut

Since photons have a non-negligible probability of converting into an e^+e^- pair, the tracking cut accounts for this possibility. The tracking cut requires that there either 0 or 2 tracks associated with each photon candidate, and when there are 2 tracks they must be consistent with a conversion pair, see Table 4.2. An additional requirement that there be no other tracks in the event is imposed. 3 events pass this selection criteria.

4.1.6 Signal Sample

The 3 candidate events are listed in Table 4.3. Comparison of the properties of these three events to ExHuME MC expectations is shown in Figures 4.1 to 4.5. Event display pictures of the 3 events are shown in Figures 4.6 to 4.8.

Run	Event	E_T (GeV)	η	$\Delta\phi$	Angle*	M (GeV/c^2)
191089	127812	6.8, 5.8	0.44, 0.19	3.00	2.5	12.7
200284	346775	5.4, 5.0	0.67, -0.07	3.09	2.6	11.2
199189	6276945	6.0, 5.1	-0.44, 0.22	3.14	3.0	11.8

Table 4.3: Details of 3 signal events. *Angle is the 3-D opening angle of the photons momenta.

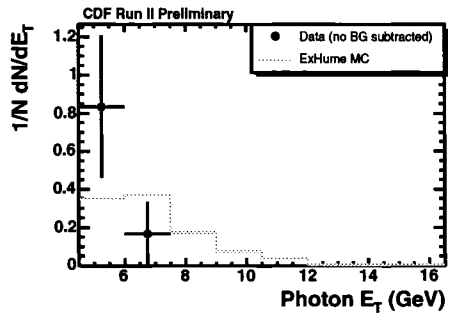

Figure 4.1: E_T of photons in signal sample (points) compared to ExHuME MC (line)

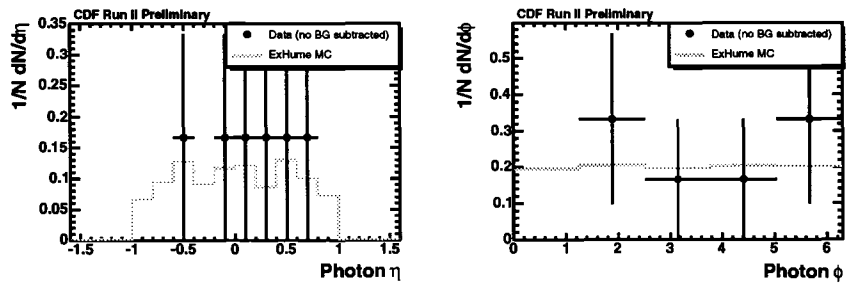

Figure 4.2: η (left) and ϕ (right) of photons in signal sample (points) compared to ExHuME MC (line)

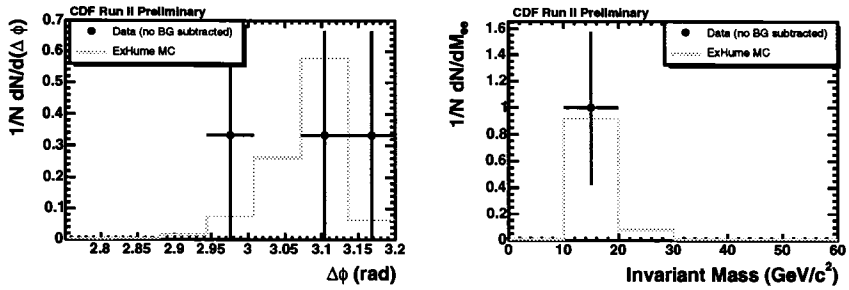

Figure 4.3: $\Delta\phi$ (left) and invariant mass (right) of photon pairs in signal sample (points) compared to ExHuME MC (line)

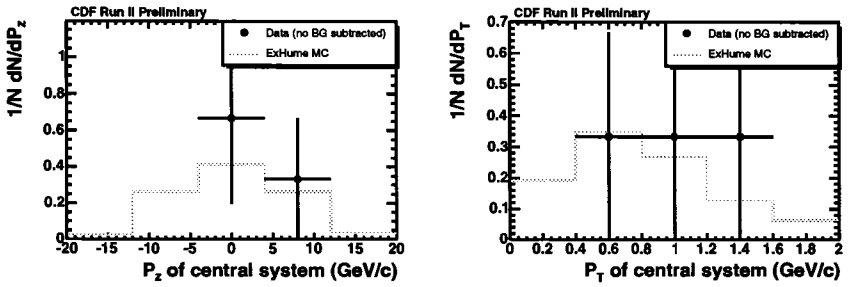

Figure 4.4: p_z and p_T of photon pairs in signal sample (points) compared to ExHuME MC (line)

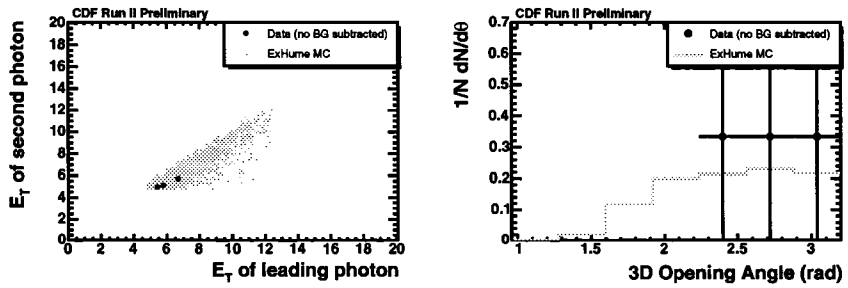

Figure 4.5: E_T vs E_T (left) and 3d opening angle of photon pairs in signal sample (points) compared to ExHuME MC (line)

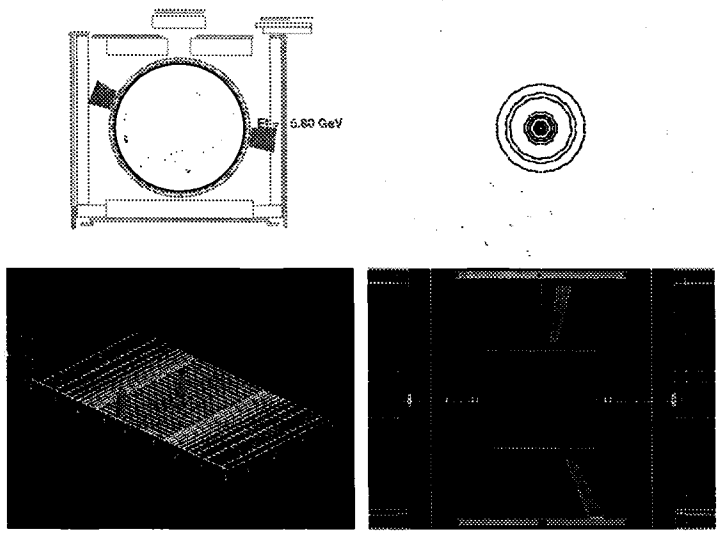

Figure 4.6: Event display of run 191089 event 127812. Note that there is no activity in the tracking chamber, and the only activity in the calorimeter is the two electromagnetic clusters.

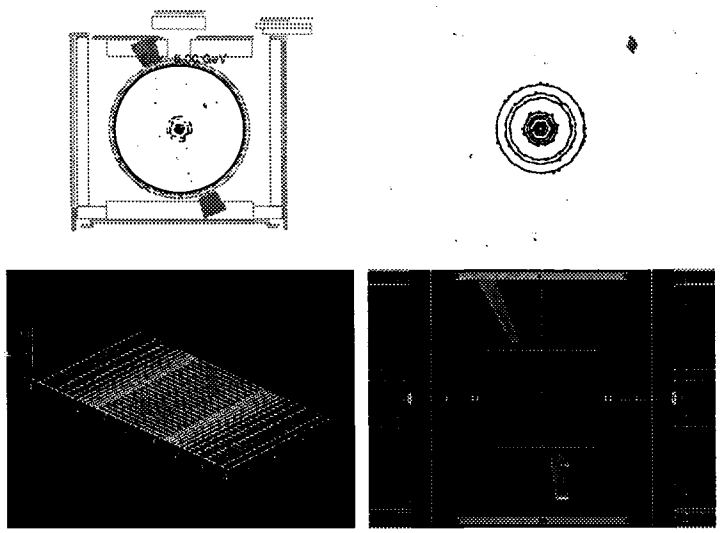

Figure 4.7: Event display of run 199189 event 6276945. Note that there is no activity in the tracking chamber, and the only activity in the calorimeter is the two electromagnetic clusters.

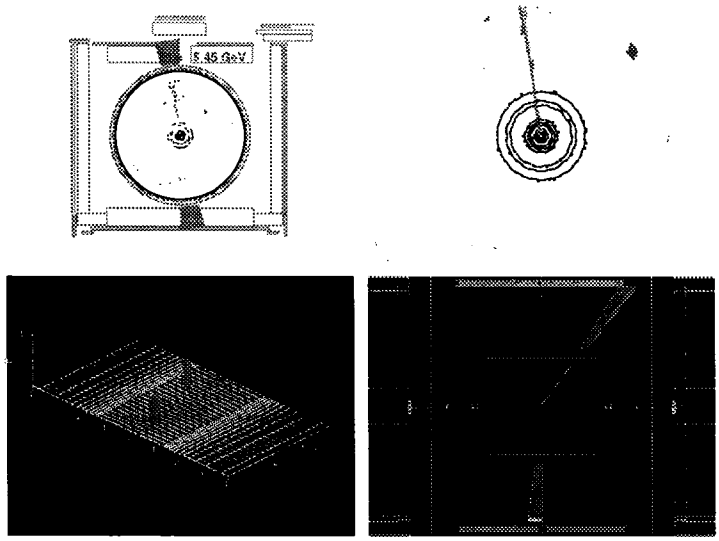

Figure 4.8: Event display of run 200284 event 346775. Note the tracks consistent with a conversion in the tracking chamber, and the only activity in the calorimeter is the two electromagnetic clusters.

4.1.7 Signal Sample Discussion

There is one interesting event that did not make it into the signal sample. The event is shown in Figure 4.9. This event looks like exclusive $\gamma\gamma$, but is excluded from the signal sample by the tracking cut. The tracks appear to be from an e^+e^- pair produced in the photon's interaction with the material of the SVX.

4.2 Efficiencies

Most of the efficiencies for this analysis are the same as the e^+e^- analysis. The two differences are the tracking efficiency is not applied, and the final state radiation efficiency is changed to the conversion efficiency, ε_{conv}, because photons do not undergo bremsstrahlung but they do convert to electron pairs and interact with the material in the tracking volume.

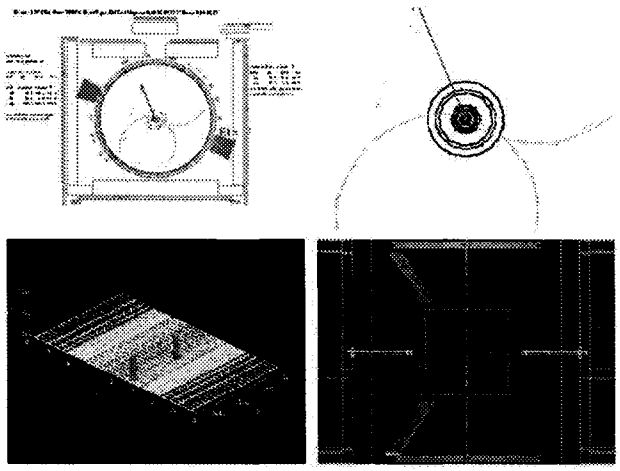

Figure 4.9: Event display of run 2000056 event 12978584 (not part of signal sample).

4.2.1 Conversion Efficiency

The conversion efficiency accounts for events that convert to e^+e^- pairs as well as events that produce electrons in the detector by Compton scattering off the tracking material. The conversion efficiency is measured by applying the exclusivity cuts to the ExHuME MC events that have been put through cdfSim version 5.3.3 and ntuplized with stntuple dev_243. Table 4.4 shows the number of events that pass each exclusive cut (starting from the number of events with 2 central photons). 2340 out of 2577 events pass all the exclusive cuts, and 2249 out of the 2340 events pass the tracking cuts. Therefore, the conversion efficiency is $\varepsilon_{conv} = 2249/2577 = 0.87$. The systematic uncertainty on this efficiency is dominated by the $\sim$10% uncertainty in material in the CDF tracking volume.

4.3 Backgrounds

The $\gamma\gamma$ and e^+e^- events are subject to the similar backgrounds. Jet fake, cosmic, exclusivity, and dissociation backgrounds all need to be accounted for.

Sample	Number of Events
Two-candidate events	2577
Pass BSC (offline)†	2577
Pass MiniPlug†	2577
Pass FwdPlug	2564
Pass MidPlug	2563
Pass EndWall	2503
Pass Central	2340
Pass Tracking	2249

Table 4.4: Number of ExHuME MC events with both photons in $|\eta| < 1$ passing exclusive cuts (sequential). †MP and BSC are not yet simulated in cdfSim.

All but the negligible cosmic background are slightly different than the e^+e^- case and are discussed in the following sections. Additional indistinguishable physics backgrounds are also discussed.

4.3.1 Jet Fake Background

The jet fake rate (F_{jet}) is the probability that a neutral hadron fakes a photon by passing the photon cuts. The most likely physics background producing this background is exclusive π°,π° where both π°'s pass the photon cuts. Since the cross section for exclusive $\pi^\circ\pi^\circ$ is not well known, the background is estimated from data, which will take into account all physics processes producing neutral hadrons. The jet fake rate for this analysis is defined as the probability that a trackless jet[1] passes the photon cuts.

$$F_{jet} \equiv \frac{N_{jets}^{pass\ photon\ cuts}(|\eta| < 1,\ NTracks = 0)}{N_{jets}(|\eta| < 1,\ NTracks = 0)} \tag{4.1}$$

Where the denominator, $N_{jets}(|\eta| < 1,\ NTracks = 0)$ is the number of jets in GAP_GAP_ST5 trigger data (the same good run list as the signal sample) with $|\eta| < 1,\ NTracks = 0$. The numerator, $N_{jets}^{pass\ photon\ cuts}(|\eta| < 1,\ NTracks = 0)$ is the number of denominator jets that pass the photon cuts listed in Table 4.1 plus the track-less cut requirement. Figure 4.10 shows F_{jet} is 3% in the 5 to 8 GeV region. Since the numerator 'jets' could actually be photons, the

[1]A trackless jet is any jet with zero tracks

CES method is used to determine what fraction of those numerator 'jets' are in fact photons. The result is that 40% of the numerator 'jets' expected to be photons. This reduces the jet fake rate estimate to 1.8%.

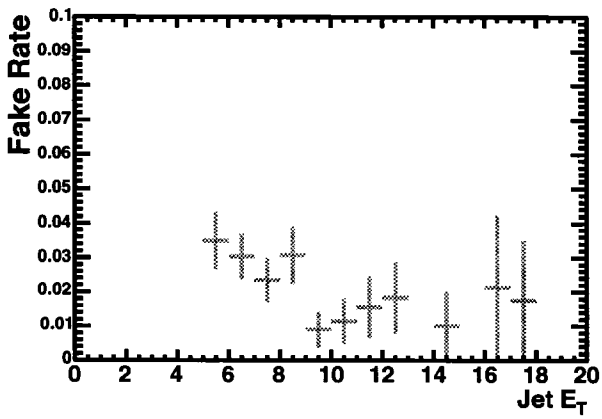

Figure 4.10: Jet fake rate (F_{jet}) is <3% before CES method correction, 1.8% after.

Similarly to the e^+e^- analysis, there are 0 events in the GAP_GAP_ST5 trigger data with two track-less jets passing the exclusive cuts for $|\eta| > 1$. Therefore, to 95% CL, there are less than 3.1 events with two track-less jets and pass the exclusive cuts. However, there is a factor 100 prescale on the GAP_GAP_ST5 trigger, therefore $N_{jj}^{pass\ all\ exc\ cuts} < 310$. Applying F_{jet} to each jet, gives $310 \cdot (0.018)^2 = 0.1$ background events. Since this estimate is an upper limit, this number will be used as a systematic on 0 background events. Therefore the jet fake background is $0^{+0.1}_{-0.0}$

4.3.2 Exclusivity Background

The exclusivity background accounts for non-exclusive events where some particle(s) passed through the cracks in the calorimetry coverage or below the noise thresholds, causing them to appear exclusive. The same methodology as the e^+e^- analysis is applied here, except that the requirement that there be no tracks (other than conversions) virtually eliminates all background events. Figure 4.11 shows that there are the three exclusive signal events, and only one

potential background event (shown in Figure 4.12). Using the same methodology as the exclusive e^+e^- analysis, the background is estimated by taking the average number of events between bins 1 and 20. This produces a background of 0.05 events. Again, since this is really an upper limit on a background, the background used for the cross section calculation will be $0.00^{+0.05}_{-0.00}$

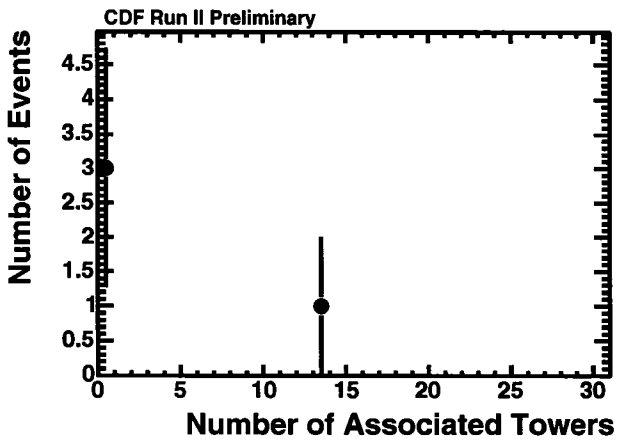

Figure 4.11: Number of associated towers in two-candidate events after tracking cut is applied.

4.3.3 Dissociation Background

The dissociation background for $\gamma\gamma$ events is expected to be lower than that of e^+e^- events because there are fewer (and higher mass) excitation states available to the proton in the exclusive QCD mechanism. Almost all N and Δ resonances are available for excitation in the QED mediated exclusive processes, while only $N(1440)$, $N(1710)$, and $N(2100)$ are available to the QCD mediated exclusive processes due to the spin selection rule. A study analagous to the e^+e^- dissociation background study was done by Sergei Striganov using the DPMJET MC [35]. The conclusion of the study was that the fraction of dissociation background events in Pomeron exchange events is 1.5%[2] This is

[2]Since DPMJET does not simulate exclusive $\gamma\gamma$, applying this study to this analysis requires that we assume there is a factorization between the dissociation of the proton and the content of the central system.

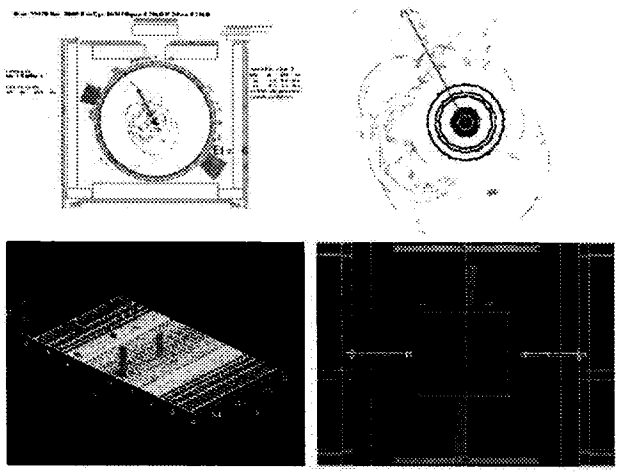

Figure 4.12: Event display of run 206669 event 3531258. This is the single background event in Figure 4.11, and looks like a $\gamma\gamma$ event with a soft interaction (exactly what the exclusivity cut is designed to eliminate).

similar to the Durham group estimation that there should be on the order of 0.1% dissociation background [20]. The DPMJET estimation corresponds to 0.05 events in the 3 event signal sample.

4.3.4 Indistinquishable Physics Processes

There are physics process other than $gg \rightarrow \gamma\gamma$ that can produce an exclusive $\gamma\gamma$ final state. KMR calculates that the contribution from quark exchange diagrams is $< 5\%$ and from $\gamma\gamma \rightarrow \gamma\gamma$ is $< 1\%$ [20]. These processes are not experimental backgrounds, they make a small contribution to the expected signal.

4.3.5 Background Summary

The sum of all background estimates discussed above is $0.0^{+0.2}_{-0.0}$. A summary of the backgrounds is shown in Table 4.5.

Background	Value
Jet Fakes	$0.0^{+0.1}_{-0.0}$ (sys)
Cosmic	neglibible
Exclusive	$0.00^{+0.05}_{-0.00}$ (sys)
Dissociation	$0.0^{+0.05}_{-0.00}$ (sys)
Total	$0.0^{+0.2}_{-0.0}$ (sys)

Table 4.5: Summary of backgrounds

Quantity	Value	Uncertainty
N_{sig}	3	$^{+2.9}_{-0.9}$ (stat)[3]
N_{bkgd}	0.0	$^{+0.2}_{-0.0}$ (sys)
$\mathscr{L}$	532	32 (sys)
ε_{exc}	0.0856	n/a
ε_{cos}	0.93	0.03 (sys)
ε_{conv}	0.87	0.09 (sys)
$\varepsilon^{\dagger}_{\gamma\gamma}$	0.57	0.07 (sys)

Table 4.6: Summary of numbers put into the cross section calculation. † is from version 2 of exclusive e^+e^- note (CDF 7930)

4.4 Cross Section

The cross section for exclusive $\gamma\gamma$ production (E_T (γ) >5 GeV, $|\eta|(\gamma) < 1$) is evaluated (using Equation 4.2 and Table 4.6) to be 0.14 $^{+0.14}_{-0.03}$ (stat) $\pm$ 0.03 (sys) pb. The Poisson probability that 0.2 events fluctuates to 3 or more events is 1.1×10^{-3}. In a one-sided normalized Gaussian distribution, the integral greater than 3.3σ is 1.1×10^{-3}. The significance of this result is therefore quoted as 3.3σ. This is the first evidence of exclusive $\gamma\gamma$ production in hadron-hadron collisions. The measured cross section is consistent with the prediction from the Durham group of 0.04 pb with an uncertainty factor of 3 to 5.

$$\sigma^{E_T>5\ GeV,|\eta|<1}_{exc,\gamma\gamma} = \frac{N_{sig} - N_{bkgd}}{\varepsilon_{conv}\varepsilon_{cos}\varepsilon_{\gamma\gamma}\varepsilon_{exc}\mathscr{L}} \tag{4.2}$$

Chapter 5

Conclusion

This thesis contains the first observation of 16 QED mediated exclusive e^+e^- events within $|\eta_e| < 2.0$ and $E_T > 5$ GeV at the CDFII detector at Fermilab. With an estimated background of $2.1\ ^{+0.6}_{-0.3}$ events, this corresponds to a 5.5σ observation (3.0×10^{-8} Poisson probability). The events are consistent in both their cross section and kinematic distributions with $pp \rightarrow p+e^+e^-+p$ through two photon exchange predicted by LPAIR MC.

The observation of a QED mediated exclusive interaction confirms that it is possible for these interactions to survive in ~TeV center of mass energy hadron-hadron collisions. This confirmation is a first step toward using QED mediated exclusive interactions for luminosity monitoring and searches for new physics at the LHC.

This thesis also reports the first evidence of QCD mediated exclusive events in hadron-hadron collisions $pp \rightarrow p+\gamma\gamma+p$. Three events were observed, with an expected background of $0.0^{+0.2}_{-0.0}$, within $|\eta_\gamma| < 1.0$ and $E_T > 5$ GeV at the CDFII detector at Fermilab. The cross section for exclusive $\gamma\gamma$ (with E_T >5 GeV, $|\eta| < 1$) is evaluated to be $0.14\ ^{+0.14}_{-0.03}$ $(stat)$ $\pm$ 0.03 (sys) pb, in agreement with the Durham group's calculation. The probability that a background of $0.0^{+0.2}_{-0.0}$ fluctuates to $\geq$3 events is 1.1×10^{-3}, corresponding to a 3.3σ observation.

Evidence that QCD mediated exclusive interactions survive in ~TeV center of mass hadron-hadron collisions means that there is potential for using these interactions to search for exclusive Higgs and other new physics at the

LHC. This observation is an important milestone for the FP420 project, whose primary objective is the installation of detectors that will make the observation of an exclusive SM Higgs possible. The fact that this observation agrees with the leading theorists in the field, the Durham group, indicates that many of the estimates the FP420 group are using are likely to be correct.

The motivation of this thesis was to test the feasibility of using exclusive production processes at the LHC to search for and measure new physics by testing predictions of exclusive production processes in ~TeV proton collisions. This goal was achieved. Theoretical predictions for both QED and QCD mediated interactions are supported with experimental evidence. If these observations help the FP420 project to its goal of using forward proton taggers at ATLAS and CMS to measure the properties of the Higgs and other new physics, than they will have had significant impact on the physics reach of the LHC. If forward proton taggers are installed, these are the first observations of physics processes that will be used by an entire focus group at both ATLAS and CMS experiments.

Bibliography

[1] Review of particle physics. *Phys. Lett.*, **B592**:1–1110, 2004.

[2] W.Greiner and J.Reinhardt. *Quantum Electrodynamics.* Springer, 2002.

[3] W.Greiner and B.Muller. *Gauge Theory of Weak Interactions.* Springer, 2000.

[4] W.Greiner and S.Schramm. *Quantum Chromodynamics.* Springer, 2004.

[5] D.Griffiths. *Introduction to Particle Physics.* Wiley, 1987.

[6] ALEPH, DELPHI, L3, OPAL, and The LEP Working Group for Higgs Searches. *Phys. Lett.*, **B565**:61, 2003.

[7] LEP Electroweak Working Group. *lepewwg.web.cern.ch/LEPEWWG/*, March 2006.

[8] S.Braccini. Two-Photon Physics at LEP. *Proceedings of IFAE*, 2003.

[9] A.Achard *et.al.* (L3 Collaboration). Muon-Pair and Tau-Pair Production in Two-Photon Collisions at LEP. *Phys.Lett*, **B585**:53–62, 2004.

[10] J.Abdallah *et al* (DELPHI Collaboration). Study of double-tagged gamma gamma events at LEPII. *Accepted by Eur. Phys. J.* **C**.

[11] C.Adler *et al.* (STAR Collaboration). Coherent ρ^0 Production in Ultra-Peripheral Heavy Ion Collisions. *Phys.Rev.Lett*, **89**:272302, 2002.

[12] J.Adams *et al.* (STAR Collaboration). Production of e^+e^- Pairs Accompanied by Nuclear Dissociation in Ultra-Peripheral Heavy Ion Collisions. *Phys.Rev.*, **C70**:031902, 2004.

[13] S.Chekanov *et al.* (ZEUS Collaboration). Exclusive electroproduction of ϕ mesons at HERA. *Nucl.Phys.*, **B718**:3–31, 2005.

[14] S.Chekanov *et al.* (ZEUS Collaboration). Exclusive electroproduction of J/ψ mesons at HERA. *Nucl.Phys.*, **B695**:3–37, 2004.

[15] T.Akesson *et al.* (AFS Collaboration). *Nucl.Phys.*, **B264**:154, 1986.

[16] J.Vermaseren. *Nucl. Phys.*, **B229**:347–371, 1983.

[17] S.Baranov. *www.desy.de/ heramc/programs/lpair/lpair.ps.gz.* 1999.

[18] L.Favart. Lepton Pair MC for HERA Physics. *Proceedings of the MC Workshop for HERA Physics*, pages 567–595, 1999.

[19] V.Khoze, A.Martin, and M.Ryskin. Prospects for New Physics Observations in diffractive processes at the LHC and Tevatron. *Eur.Phys.J*, **C23**:311, 2002.

[20] V.Khoze, A.Martin, M.Ryskin, and J.Stirling. Diffractive $\gamma\gamma$ Production at Hadron Colliders. *Eur.Phys.J*, **C38**:475, 2005.

[21] A.Kaidalov, V.Khoze, A.Martin, M.Ryskin, and J.Stirling. Central exclusive diffractive production as a spin–parity analyser: from hadrons to Higgs. *Eur.Phys.J*, bf C31:387, 2003.

[22] A.Kaidalov, V.Khoze, A.Martin, M.Ryskin, and J.Stirling. Extending the study of the Higgs sector at the LHC by proton tagging. *Eur.Phys.J*, **C33**:261, 2004.

[23] J.Collins. Sudakov form factors. *Adv.Ser.Direct.High Energy Phys.*, **5**:573–614, 1989.

[24] J.Monk and A.Pilkington. ExHuME: A Monte Carlo Event Generator for Exclusive Diffraction. hep-ph/0502077, 2005.

[25] P.Collins. *Introduction to Regge Theory and high Energy Physics.* Cambridge University Press, 1977.

[26] B.Caron and J.Pinfold. Experimental aspects of luminosity determination at the lhc: Lepton pair and single gauge boson production. *Proceedings on Workshop on Forward Physics and Luminosity Dertmination at the LHC*, World Scientic, Helsinki 2000.

[27] M.Albrow and A.Rostovtsev. Searching for the higgs at hadron colliders using the missing mass method. *FERMILAB-PUB-00-173*, 2000.

[28] B.Cox. A review of forward proton tagging at 420m at the LHC, and relevant results from the Tevatron and HERA. *Talk at HCP2004*, 2004.

[29] V.Khoze, A.Martin, M.Ryskin, and J.Stirling. Hunting a light CP-violating Higgs via diffraction at the LHC. *Eur.Phys.J*, **C34**:2327, 2004.

[30] B.Cox *et al.* Observing a light CP violating Higgs boson in diffraction. *Phys.Rev.*, **D68**:075004, 2003.

[31] Forward Proton Taggers at 420m Project. *www.fp420.com.*

[32] M.G.Albrow et al. A Search for the Higgs Boson using Very Forward Tracking Detectors with CDF. *hep-ex/0511057*, 2001.

[33] CDF II Collaboration. *The CDFII Technical Design Report.* FERMILAB-Pub-96-390-E, http://www-cdf.fnal.gov/internal/upgrades/tdr/tdr.html.

[34] V.Khoze and M.Ryskin. Private Communication. May, 2006.

[35] J.Ranft. *DPMJET vII.5.* hep-ph/9911232, 1999.